




Extreme rogue wave generation from narrowband partially coherent wavesD. S. Agafontsev ^{1,2,*}, S. Randoux ³, and P. Suret ³¹*P. P. Shirshov Institute of Oceanology of RAS, 36 Nakhimovsky prospekt, Moscow 117997, Russia*²*Skolkovo Institute of Science and Technology, 121205 Moscow, Russia*³*Laboratoire de Physique des Lasers, Atomes et Molecules, UMR-CNRS 8523, Université de Lille, Cité Scientifique, 59655 Villeneuve d'Ascq Cedex, France*

(Received 20 December 2020; accepted 1 March 2021; published 22 March 2021)

In the framework of the focusing one-dimensional nonlinear Schrödinger equation, we study numerically the integrable turbulence developing from partially coherent waves (PCW), which represent superposition of uncorrelated linear waves. The long-time evolution from these initial conditions is characterized by emergence of rogue waves with heavy-tailed (non-Gaussian) statistics, and, as was established previously, the stronger deviation from Gaussianity (i.e., the higher frequency of rogue waves) is observed for narrower initial spectrum. We investigate the fundamental limiting case of very narrow initial spectrum and find that shortly after the beginning of motion the turbulence enters a quasistationary state (QSS), which is characterized by a very slow evolution of statistics and lasts for a very long time before arrival at the asymptotic stationary state. In the beginning of the QSS, the probability density function (PDF) of intensity turns out to be nearly independent of the initial spectrum and is very well approximated by a certain Bessel function that represents an integral of the product of two exponential distributions. The PDF corresponds to the maximum possible stationary value of the fourth-order moment of amplitude $\kappa_4 = 4$ and yields a probability to meet intensity above the rogue wave threshold that is higher by 1.5 orders of magnitude than that for a random superposition of linear waves. We routinely observe rogue waves with amplitudes ten times larger than the average one, and all of the largest waves that we have studied are very well approximated by the amplitude-scaled rational breather solutions of either the first (Peregrine breather) or the second orders.

DOI: [10.1103/PhysRevE.103.032209](https://doi.org/10.1103/PhysRevE.103.032209)**I. INTRODUCTION**

The phenomenon of rogue waves—extremely large waves that appear unpredictably from moderate wave background—has been intensively studied in recent years; see, e.g., Refs. [1–3] and also the recent review [4]. One of the basic nonlinear mathematical models suitable for the description of such waves is the one-dimensional nonlinear Schrödinger equation (1D-NLSE) of the focusing type,

$$i\psi_t + \psi_{xx} + |\psi|^2\psi = 0, \quad (1)$$

where t is time, x is spatial coordinate, and ψ is the wave-field envelope. Several exact solutions of this equation were suggested as candidates for rogue waves, including the Peregrine [5] and Akhmediev [6,7] breathers, Kuznetsov-Ma solitons [8,9], and super-regular breathers [10]. Taking specific and carefully designed initial conditions, these solutions were reproduced in well-controlled experiments performed in different physical systems [11–17].

With what frequency such solutions appear in nature, however, is a different question; for instance, typical oceanic waves represent weakly nonlinear objects having nearly Gaussian statistics; see, e.g., Refs. [2,3,18]. This implies that the problem of rogue waves should be examined in the context

of random initial conditions, and the key characteristic for the study should be the probability density function (PDF) of waves' amplitude, or, alternatively, the PDF $\mathcal{P}(I)$ of relative wave intensity $I = |\psi|^2 / \langle |\psi|^2 \rangle$, where $\langle |\psi|^2 \rangle$ is the average intensity. Of particular interest is comparison of the PDF for a nonlinear system with the exponential PDF,

$$\mathcal{P}_R(I) = e^{-I}, \quad (2)$$

which describes distribution of intensity for a superposition of uncorrelated linear waves and corresponds to Gaussian PDFs for the real $\text{Re } \psi$ and imaginary $\text{Im } \psi$ parts of the wave-field and Rayleigh PDF for the amplitude $|\psi|$; see, e.g., Refs. [19, chapter 5] and [20, chapter 3]. In nonlinear systems, the phases of Fourier modes composing the wave field may correlate, which in turn may lead to enhanced appearance of large waves. Throughout the paper, we use the distribution (2) as a benchmark, allowing us to compare the frequency of large waves for the examined system with that for a linear one.

Note that, in the context of optical waves, the intensity is a natural quantity of interest. However, it can also be relevant in water wave experiments by using the Hilbert transform of the wave form to extract the slow varying amplitude; see, e.g., Ref. [21].

The 1D-NLSE is integrable in terms of the inverse scattering transform (IST) method [22,23]. Statistical analysis of integrable systems with random input is the concept of *integrable turbulence*, first introduced by Zakharov in Ref. [24].

*dmitrij@itp.ac.ru

Integrability implies conservation of infinite series of invariants (integrals of motion), and since these invariants are different for different types of initial conditions, the wave statistics should depend on the statistics of the input random process even over a long time.

In particular, for the scenario of the noise-induced modulational instability (MI) of a plane wave (the condensate), the PDF coincides over a long time with the exponential distribution (2); see Refs. [25,26]. This result was later generalized for the MI of cnoidal waves [27], with demonstration that (depending on parameters of the unstable cnoidal wave) either the PDF is sufficiently close to the exponential distribution or the dynamics reduces to two-soliton collisions which occur with exponentially small rate. For both the condensate and the cnoidal wave initial conditions, the development of the MI leads to integrable turbulence, which approaches asymptotically its *stationary state*—the state in which its statistical characteristics are independent of time.

Meanwhile, for the partially coherent wave (PCW) initial conditions, which represent superpositions of uncorrelated linear waves and are characterized by the exponential distribution of intensity (2), the results were shown to be completely different [28]. The integrable turbulence in this case quickly reaches a state in which its statistical characteristics do not change visibly, and the PDF in this state exceeds the exponential distribution (2) by orders of magnitude at large intensities (see also earlier studies [29–31] for the long-crested water waves of JONSWAP spectrum). Moreover, as was demonstrated in Refs. [32–36], the excess over the exponential PDF is larger for the initial conditions of larger correlation length or larger average intensity that are equivalent to those of the narrower initial spectrum. Note that the transition between the two types of initial conditions—i.e., from the condensate perturbed by small initial noise to the PCW—was widely investigated in Refs. [32,33], in particular, with the help of the IST methods.

In the present paper, with the help of extensive numerical simulations, we study in detail the fundamental limiting case when the integrable turbulence develops from PCW of narrowband spectrum and its long-time statistics exhibits the strongest deviation from Gaussianity. For the narrow initial spectrum, the influence of the group velocity dispersion is weak, so that initially the nonlinear effects prevail over the linear dispersive ones. As a natural criterion for narrowness, we therefore demand the initial nonlinearity strength α_0 , that is, the dimensionless ratio of the potential energy to the kinetic one, to be large:

$$\alpha_0 = \frac{|H_{nl}|}{H_l} \Big|_{t=0} = \frac{\langle |\psi|^2 \rangle}{\delta k^2} \Big|_{t=0} \gg 1. \quad (3)$$

Here the potential energy H_{nl} is related to the nonlinear term of the 1D-NLSE and the kinetic energy H_l is related to (linear) dispersion [see Eqs. (9) and (10) below], and, as we explain later, the initial nonlinearity strength α_0 equals the average intensity $\langle |\psi|^2 \rangle$ divided by the mean square spectral width δk^2 . Thus, in dimensionless variables, the studied case of narrow initial spectrum is equivalent to large intensity, and from comparison with results of Ref. [34] it appears to be one of the most promising for extreme generation of rogue waves.

We demonstrate that turbulence developing from narrowband PCW relatively quickly enters a state, which we call *quasistationary* (QSS). In the QSS, most of the basic statistical functions (e.g., the moments and PDF of intensity) change with time very slowly, while some other higher order statistical functions, most notably the autocorrelation of intensity, continue to evolve noticeably. The subsequent evolution toward the asymptotic *stationary* state turns out to be very long. For these two reasons—the slow evolution of statistics in the QSS and a very distant stationary state—we believe that, for any possible practical application, examination of the QSS is important, so that we concentrate on it, focusing on the kinetic and potential energies, the moments, and the PDF of intensity.

In particular, we show that, in the QSS, the ratio of the potential energy to the kinetic one (the nonlinearity strength) α_{QSS} and the fourth-order moment $\kappa_4 = \langle |\psi|^4 \rangle / \langle |\psi|^2 \rangle^2$ increase monotonically for vanishing initial spectral width $\delta k \rightarrow 0$ (i.e., increasing initial nonlinearity $\alpha_0 \rightarrow +\infty$), but turn out to be bounded from above, $\alpha_{QSS} \leq 2$ and $\kappa_4 \leq 4$. Hence, by demanding narrowness of the initial spectrum, we obtain the integrable turbulence that develops with the maximum nonlinearity $\alpha_{QSS} \approx 2$ and the maximum fourth-order moment $\kappa_4 \approx 4$, possible for the PCW initial conditions.

We find that, in the beginning of the QSS, the PDF does not depend on the shape of the initial spectrum and slightly varies with initial nonlinearity α_0 . The close-to-universal profile of the PDF exceeds the exponential distribution (2) by orders of magnitude at large intensities and is very well approximated by a certain Bessel function representing an integral of the product of two exponential distributions. The Bessel function corresponds to the fourth-order moment $\kappa_4 = 4$ and yields the probability of meeting intensity above the rogue wave threshold, $I > 8$, by 1.5 orders of magnitude higher than the exponential distribution (2). To our knowledge, these values of the fourth-order moment and the frequency of rogue waves, observed in our numerical simulations, are the largest that have been reached so far for (quasi)stationary states of the 1D-NLSE developing from various types of initial conditions. We routinely detect rogue waves 10 times larger than the average amplitude, and all of the largest waves that we have studied are very well approximated by the amplitude-scaled rational breather solutions of either the first (the Peregrine breather) or the second orders.

The paper is organized as follows. In the next section, we give a general overview for the problem of integrable turbulence developing from narrowband PCW. In Sec. III, we describe our numerical methods. In Sec. IV, we discuss the basic features of evolution from which we conclude existence of the QSS, and in Sec. V, we report our results for its statistical properties, focusing on the moments and PDF of intensity. The final section contains conclusions. The paper has also several Appendixes, where we discuss scaling transformations of the 1D-NLSE, construct a nonsymmetric initial spectrum, consider properties of the wave-action spectrum and the autocorrelation of intensity, and study effects of inclusion of an additional wide-spectrum noise to the initial conditions, as it might be important for practical applications.

II. PARTIALLY COHERENT WAVES OF NARROWBAND SPECTRUM

We study evolution governed by the focusing 1D-NLSE (1) starting from initial conditions of fixed average intensity,

$$\psi|_{t=0} = \psi_0(x), \quad \overline{|\psi_0|^2} = \frac{1}{L} \int_{-L/2}^{L/2} |\psi_0|^2 dx = N. \quad (4)$$

Here the overline denotes spatial averaging, N is constant, and for the numerical study we consider the periodic problem $x \in [-L/2, L/2]$ with a very large period $L \gg 1$. The initial conditions are given by a discrete sum of Fourier components,

$$\psi_0(x) = \sum_k \psi_{0k} e^{ikx}, \quad \psi_{0k} = \sqrt{N_k} e^{i\phi_k}, \quad (5)$$

where $k = 2\pi m/L$ is the wave number, $m \in \mathbb{Z}$ is integer, $N_k \geq 0$ is a (given) smooth function of k , and $\phi_k \in [0, 2\pi)$ are random phases. We use the so-called random phase (RP) model (see, e.g., Ref. [19], in which only the phases ϕ_k are considered to be random and uncorrelated) and average our results over the ensemble of phase realizations.

As an integrable equation, the 1D-NLSE conserves an infinite series of integrals of motion, and the first three of these invariants are wave action (which in our notation equals the average intensity)

$$N = \overline{|\psi|^2} = \frac{1}{L} \int_{-L/2}^{L/2} |\psi|^2 dx = \sum_k |\psi_k|^2, \quad (6)$$

momentum

$$P = \frac{i}{2L} \int_{-L/2}^{L/2} (\psi_x^* \psi - \psi_x \psi^*) dx = \sum_k k |\psi_k|^2, \quad (7)$$

and total energy

$$E = H_l + H_{nl}, \quad (8)$$

$$H_l = \overline{|\psi_x|^2} = \frac{1}{L} \int_{-L/2}^{L/2} |\psi_x|^2 dx = \sum_k k^2 |\psi_k|^2, \quad (9)$$

$$H_{nl} = -\frac{\overline{|\psi|^4}}{2} = -\frac{1}{2L} \int_{-L/2}^{L/2} |\psi|^4 dx. \quad (10)$$

Here H_l is the kinetic energy (linear contribution), H_{nl} is the potential energy (nonlinear contribution), and ψ_k is the Fourier-transformed wave field,

$$\psi_k(t) = \frac{1}{L} \int_{-L/2}^{L/2} \psi(t, x) e^{-ikx} dx.$$

According to the central limit theorem, the PDF of intensity for the initial conditions (4) and (5) is the exponential distribution (see, e.g., Refs. [19, chapter 5] and [20, chapter 3]),

$$\mathcal{P}_R(|\psi_0|^2) = \frac{1}{N} \exp\left(-\frac{|\psi_0|^2}{N}\right). \quad (11)$$

This allows us to find the ensemble-averaged potential energy,

$$\begin{aligned} \langle H_{nl} \rangle|_{t=0} &= -\frac{1}{2} \overline{|\psi_0|^4} \\ &= -\frac{1}{2} \int_0^{+\infty} |\psi_0|^4 \mathcal{P}_R(|\psi_0|^2) d|\psi_0|^2 = -N^2, \end{aligned} \quad (12)$$

and the fourth-order moment,

$$\kappa_4|_{t=0} = \frac{\overline{|\psi_0|^4}}{(\overline{|\psi_0|^2})^2} = 2, \quad (13)$$

where $\langle \dots \rangle$ means averaging over the ensemble of random phases.

As follows from Eqs. (6) and (9), the square spectral width can be defined as the ratio of the kinetic energy to the average intensity (wave action),

$$\delta k^2 = \frac{\sum_k k^2 |\psi_k|^2}{\sum_k |\psi_k|^2} = \frac{H_l}{N}. \quad (14)$$

Together with Eq. (12), this yields the initial nonlinearity strength that equals the average intensity $N = \langle |\psi|^2 \rangle$ divided by the square spectral width δk^2 ,

$$\alpha_0 = \frac{|\langle H_{nl} \rangle|}{H_l}|_{t=0} = \frac{\langle |\psi|^2 \rangle}{\delta k^2}|_{t=0}. \quad (15)$$

The problem of evolution within the focusing 1D-NLSE with arbitrary coefficients before dispersion and nonlinearity terms, that starts from initial conditions of arbitrary average intensity, can be renormalized to Eq. (1) and initial conditions of unit average intensity $N = 1$; see Appendix A for detail. In dimensional variables, in which the dispersion and nonlinearity coefficients do not equal to unity, the second equality in relation (15) is changed with proportionality. The advantage of criterion $\alpha_0 \gg 1$ for narrowness of the initial spectrum comes from dimensionless nature of the quantity α_0 , which can be computed readily using the dimensional definitions for kinetic and potential energies. For this reason, throughout the paper we use the nonlinearity strength α_0 as a characteristic of the spectral width δk , instead of setting the spectral width directly.

In the following, without loss of generality, we consider evolution governed by the 1D-NLSE (1) starting from initial conditions (4) of unit average intensity, $N = 1$. Then, the initial ensemble-averaged potential energy equals to minus unity, $\langle H_{nl} \rangle = -1$, and the kinetic energy equals the square spectral width, $H_l = \delta k^2$, so that the initial nonlinearity is connected with the spectral width as $\alpha_0 = \delta k^{-2}$. For narrowness of the initial spectrum we demand $\alpha_0 \gg 1$, and when we consider different (dimensionless) spectral widths δk , we set them through the only parameter—the initial nonlinearity α_0 .

To summarize, we examine evolution governed by the 1D-NLSE (1) starting from random superpositions of uncorrelated linear waves (4) and (5) with unit average intensity, $N = 1$, and of narrowband spectrum, $\delta k^2 \ll 1$. Such initial conditions are characterized by the exponential distribution of intensity (11), have small kinetic energy, $H_l = \delta k^2 \ll 1$, and potential energy of minus unity, $\langle H_{nl} \rangle = -1$, so that they are highly nonlinear, $\alpha_0 = |\langle H_{nl} \rangle|/H_l = 1/\delta k^2 \gg 1$. The total

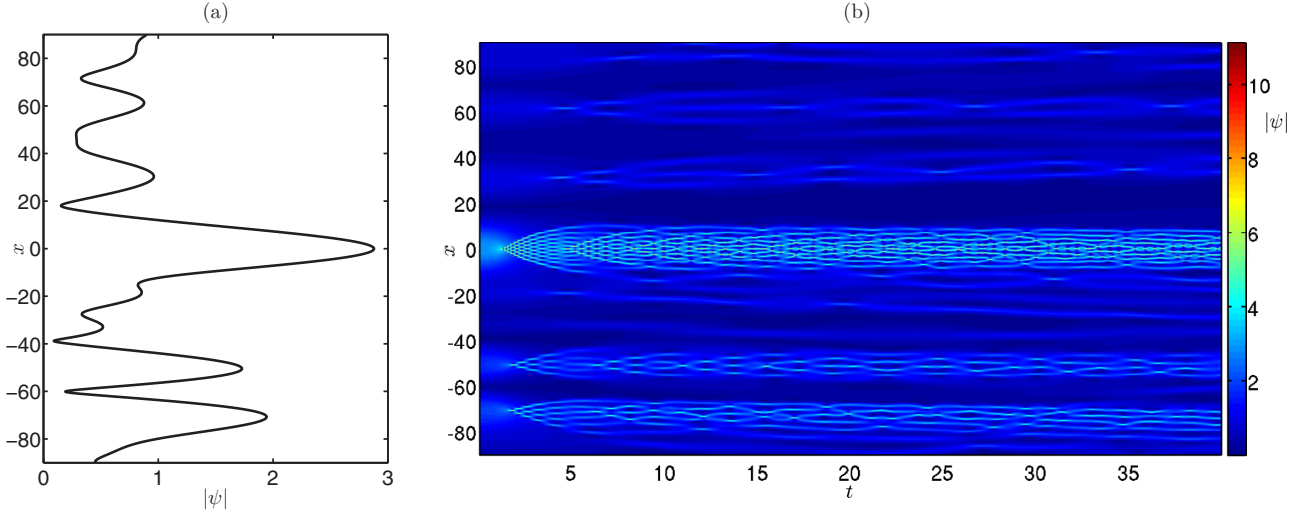


FIG. 1. (a) Initial amplitude $|\psi|$ and (b) space-time evolution for one realization of a PCW of narrowband spectrum. The initial spectrum is super-Gaussian with the exponent $n = 32$ and nonlinearity strength $\alpha_0 = 64$. The maximum of the initial amplitude is shifted to $x = 0$ for better visualization.

energy is close to minus unity, $\langle E \rangle = -1 + 1/\alpha_0 \approx -1$, and the fourth-order moment equals two, $\kappa_4 = 2$. In the physical space, each realization represents a collection of humps of characteristic width $\delta x \simeq 1/\delta k = \sqrt{\alpha_0} \gg 1$; see Fig. 1(a). The linear timescale for the problem is large, $t_l = \delta x^2 \simeq \alpha_0 \gg 1$, and the nonlinear timescale equals unity, $t_{nl} = 1$; see, e.g., Ref. [37].

The described initial conditions resemble a plane wave in the sense of small spectral width. However, importantly, a plane wave cannot be obtained from them in the limit $\delta k \rightarrow 0$, as it has different total energy $E = -1/2$ and δ -distribution of intensity.

Note that in our dimensionless formulation the fourth-order moment equals the double absolute value of the potential energy,

$$\kappa_4 = 2|\langle H_{nl} \rangle|; \quad (16)$$

see Eqs. (4), (10), and (13). When we start from initial conditions of small spectral width, $\delta k \ll 1$, we expect the latter to increase to some value of unity order during the evolution in time. This means increase in the kinetic energy $H_l = \delta k^2$ to some value of unity order as well, see Eq. (14), and, due to conservation of the total energy, the same increase in the absolute value of the potential energy. The latter equals unity at the initial time, $|\langle H_{nl} \rangle| = 1$, that corresponds to the fourth-order moment $\kappa_4 = 2$; see Eq. (16). Hence, with increase of the spectral width during the evolution, we also expect the fourth-order moment to significantly increase from the value of 2, which would correspond to strongly nonexponential PDF and enhanced probability of rogue wave events. These ideas, exploiting connection between the spectral width, the fourth-order moment, and the probability of rogue wave appearance, were suggested in Ref. [38] and can be generalized for a class of NLS-type equations in multiple spatial dimensions.

In the present paper, we focus on examination of the ensemble-average kinetic $\langle H_l(t) \rangle$ and potential $\langle H_{nl}(t) \rangle$ energies, the moments of amplitude $M^{(p)}(t) = \langle |\psi|^p \rangle$ and, in particular, the fourth-order moment $\kappa_4 = M^{(4)}$, and the PDF

$\mathcal{P}(I, t)$ of intensity $I = |\psi|^2$. In Appendix C we also consider the other two important statistical functions: the wave-action spectrum and the autocorrelation of intensity. For the PDF, we use normalization $\int \mathcal{P}(I) dI = 1$. In the next sections, we will also use that the exponential PDF (2) corresponds to the following values of the moments,

$$M_R^{(p)} = \int_0^{+\infty} |\psi|^p \mathcal{P}_R(|\psi|^2) d|\psi|^2 = \Gamma_{1+p/2}, \quad (17)$$

where Γ is the Gamma function.

The ensemble-averaged statistical functions depend in our problem on one free parameter, the function N_k , defining the initial spectrum in Eq. (5); for unit average intensity $N = 1$, this function has constraint $\sum_k N_k = 1$ [see Eq. (6)]. In the following, we artificially split this parameter by two: (i) the spectral width, which we set through the nonlinearity strength and consider to be small, $\delta k = 1/\sqrt{\alpha_0} \ll 1$, and (ii) the shape of the function N_k , for instance, Gaussian or super-Gaussian.

III. NUMERICAL METHODS

We integrate Eq. (1) numerically in a large box $x \in [-L/2, L/2]$, $L \gg 1$, with periodic boundaries; the specific choice of the box size for different experiments is explained below. We use the pseudospectral Runge-Kutta fourth-order method in an adaptive grid, with the grid step Δx set for the analysis of the Fourier spectrum of the solution; see Ref. [25] for details. We have checked that the first 10 integrals of motion of the 1D-NLSE are conserved by our numerical scheme up to the relative errors from 10^{-10} (the first three invariants) to 10^{-6} (the tenth invariant) orders.

As initial conditions, we use PCW with super-Gaussian Fourier spectrum

$$\psi_0(x) = \sum_k A_k^{(0)} e^{ikx + i\phi_k}, \quad (18)$$

$$A_k^{(0)} = \left(\frac{C_n}{\theta L} \right)^{1/2} e^{-|k|^n / \theta^n}, \quad (19)$$

where θ plays the role of the spectral width (14), $\theta \simeq \delta k$, ϕ_k are random phases for each k and each realization of the initial conditions, $n \in \mathbb{N}$ is the exponent defining shape of the initial spectrum, and $C_n = \pi 2^{1/n} / \Gamma_{1+1/n}$ is the normalization constant such that the average intensity is unity, $|\overline{\psi_0(x)}|^2 = 1$; see, e.g., Eq. (20) below. For each pair of parameters n and θ , we perform simulations for an ensemble of 1000 random realizations of phases ϕ_k and then average the results over these realizations. The initial kinetic energy is proportional to θ^2 ,

$$\begin{aligned} H_I|_{t=0} &= \frac{1}{L} \int_{-L/2}^{+L/2} |\psi_{0x}|^2 dx \\ &= \frac{C_n}{\theta L} \sum_k k^2 e^{-2k^n/\theta^n} \approx \frac{\Gamma_{1+3/n}}{\Gamma_{1+1/n}} \frac{\theta^2}{3 \times 2^{2/n}}, \end{aligned} \quad (20)$$

while the initial ensemble-averaged potential energy equals to minus unity; see Eq. (12). Thus, the initial nonlinearity α_0 is inversely proportional to θ^2 ,

$$\frac{1}{\delta k^2} = \alpha_0 = \frac{|\langle H_{nl} \rangle|}{\langle H_I \rangle} \approx \frac{\Gamma_{1+1/n} 3 \times 2^{2/n}}{\Gamma_{1+3/n} \theta^2}. \quad (21)$$

We perform simulations for several profiles of the initial spectrum (19), including exponential $n = 1$, Gaussian $n = 2$, and super-Gaussian $n = 8$ and $n = 32$, and also for several initial nonlinearity levels α_0 from 1 to 256, with the parameter θ determined from Eq. (21). We also study generic (nonsymmetric) Fourier spectra $A_k^{(0)}$ in Eq. (18), which we construct as described in Appendix B. The distance between neighbor harmonics in our simulations depends only on the box size, $\Delta k = 2\pi/L$, and we choose the box sufficiently large, $L \geq 512\pi$, so that the region in the k space $[-\theta, \theta]$, containing most of the initial wave action, see Eq. (6), is resolved with at least

$$2\theta/\Delta k \gtrsim 30 \quad (22)$$

harmonics. We have confirmed that simulations performed in twice larger boxes L provide the same statistical results. Additionally, we have checked that simulations with smaller boxes, for which the region $[-\theta, \theta]$ is resolved with just $2\theta/\Delta k \simeq 20$ harmonics, also give us very similar results, meaning that this relatively small number of uncorrelated modes is sufficient to reproduce our results in practice.

IV. TIME EVOLUTION AND THE QUASISTATIONARY STATE

Some insights into the initial stage of evolution of a PCW having a narrowband spectrum ($\alpha_0 \gg 1$) are provided by the so-called *semiclassical limit* (or the *zero-dispersion limit*) of the 1D-NLSE, that reads as

$$i\varepsilon\psi_\tau + \frac{\varepsilon^2}{2}\psi_{\zeta\zeta} + |\psi|^2\psi = 0. \quad (23)$$

Here $\varepsilon = \sqrt{t_{nl}/t_l} \simeq 1/\sqrt{\alpha_0}$ is a small parameter, $t_l \gg t_{nl}$ are linear and nonlinear timescales, and $\zeta = \varepsilon x/\sqrt{2}$ and $\tau = \varepsilon t$ are renormalized space and time.

Within this normalization, the subsequent application of the Madelung transform results in equations of motion for

one-dimensional fluid [39], which contain terms proportional to ε^2 . For initial conditions in the form of a single smooth hump with width and height of unity order, $\delta\zeta \approx 1$ and $|\psi| \approx 1$, these terms can be neglected at the early stage of evolution. However, without these terms at later stages, there exists a certain (critical) time of unity order, $\tau \approx 1$, when the gradient of the solution explodes (the *gradient catastrophe*). As has been rigorously demonstrated in Ref. [40], in the full equation (23) the gradient catastrophe is regularized by emergence of a coherent structure, which tends locally to the Peregrine breather solution [5] as $\varepsilon \rightarrow 0$. The subsequent optical fiber experiments [41] have shown that this scenario is robust and can be observed for the parameter ε as large as 0.4. Importantly, in variables (x, t) , regularization of the gradient catastrophe and emergence of the Peregrine-like coherent structure arise for the time $t \sim 1/\varepsilon \simeq \sqrt{\alpha_0}$.

A PCW of narrowband spectrum represents a collection of humps of characteristic width $\delta x \simeq 1/\delta k = \sqrt{\alpha_0}$; in variables (ζ, τ) , these humps have width and height of unity order, $\delta\zeta \sim 1$ and $|\psi| \sim 1$. At the early stage of evolution, each individual hump may lead to local emergence of the Peregrine-like coherent structure at its own critical time. A detailed numerical study with demonstration of this scenario has been performed in Ref. [42], and it has been shown that the time when the fourth-order moment κ_4 takes maximum value turns out to be also of unity order, $\tau_m \sim 1$, and corresponds to the maximum presence of the Peregrine-like coherent structures appearing on top of different humps. Hence, in our variables (x, t) , this time has scaling with the nonlinearity strength α_0 as $t_m = \tau_m/\varepsilon \sim 1/\varepsilon \simeq \sqrt{\alpha_0}$.

The theory developed for the semiclassical limit of the 1D-NLSE provides insights into the early stage of evolution of a narrowband PCW [42–44], for $t \lesssim \sqrt{\alpha_0}$. In the present paper, we investigate statistics for the subsequent stage, $t \gtrsim \sqrt{\alpha_0}$.

Figure 1 illustrates the typical space-time evolution developing from a PCW, on the example of numerical experiment with super-Gaussian initial spectrum (19) with the exponent $n = 32$ and nonlinearity strength $\alpha_0 = 64$. As shown in Fig. 1(a), the PCW looks like a collection of humps of characteristic width $\delta x \simeq 1/\delta k = \sqrt{\alpha_0} \simeq 10$. The spatiotemporal dynamics from this initial condition, demonstrated in Fig. 1(b), reveals that each hump experiences an individual self-focusing evolution that shortly after beginning of motion leads to emergence of a coherent structure at the top of the hump. The coherent structure reaches a maximum amplitude about three times larger than the initial one and then disappears with formation of two new breather-like structures on its left and right sides. The two structures then also reach maximum amplitudes and disappear with emergence of three breather-like structures—one in between and the other two on the left and right sides. This process continues, and, for the largest hump, the breather-like structures fill the entire area to time $t \simeq 5$. The smaller humps repeat the described scenario for the largest hump, but with longer characteristic times (compare the dynamics for the humps centered at $x \simeq -50$ and $x \simeq -70$ with that for $x = 0$). Note that, even after sufficiently long evolution, the breather-like structures tend to stay within the initial area of the humps, which corroborates the suggestion of independence of the humps at the early stages of motion [42]. In the following, we concentrate on

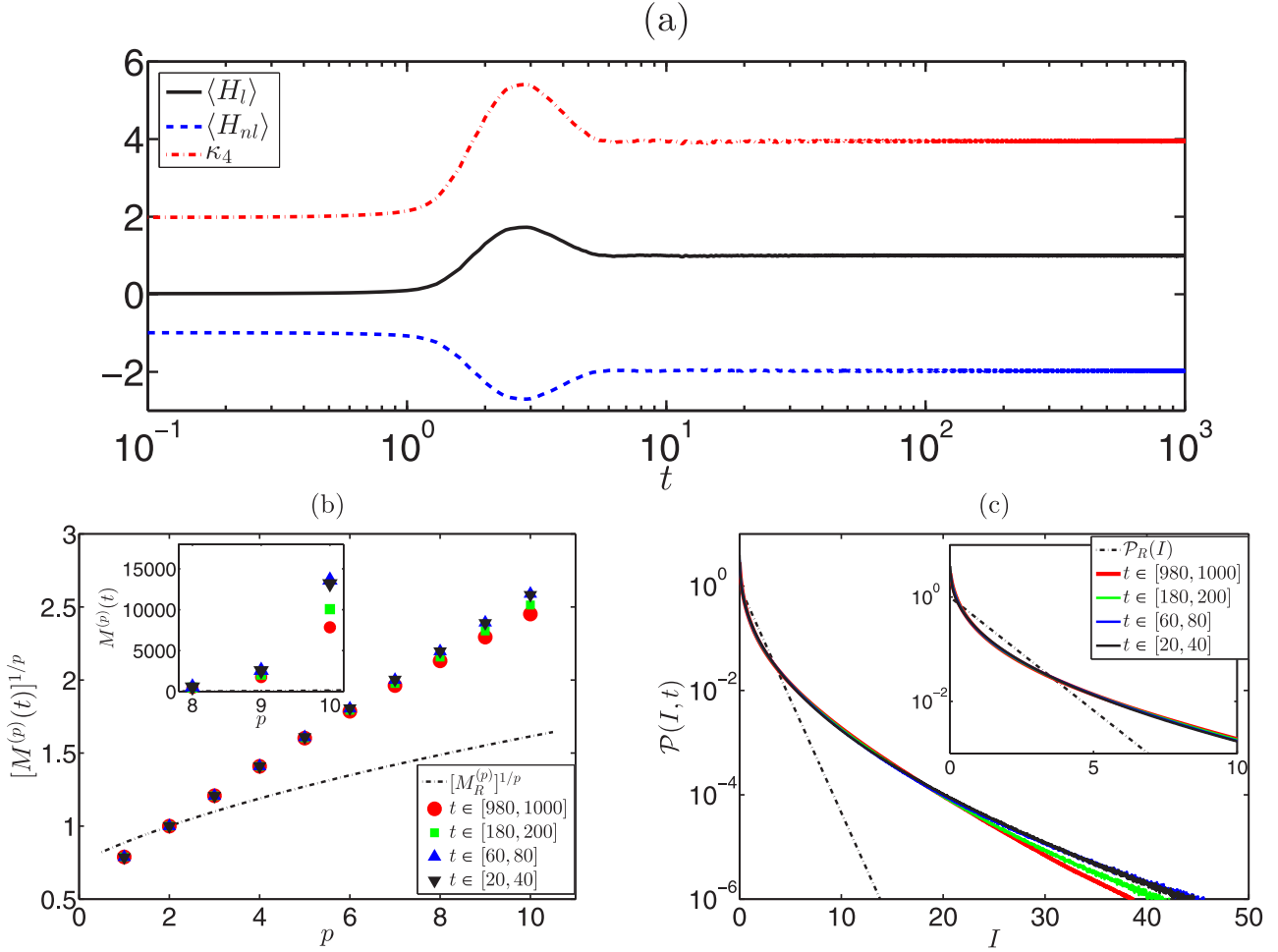


FIG. 2. (a) Evolution of the ensemble-averaged kinetic energy $\langle H_l \rangle$, potential energy $\langle H_{nl} \rangle$, and the fourth-order moment κ_4 ; note the logarithmic horizontal scale. [(b), (c)] Averaged over ensemble and different time intervals statistical functions: (b) the moments $[M^{(p)}]^{1/p}$ and (c) the PDF $\mathcal{P}(I)$. The initial spectrum is super-Gaussian with the exponent $n = 32$ and nonlinearity strength $\alpha_0 = 64$. The inset in panel (b) shows the higher order moments $M^{(p)}$ (without the $1/p$ power), while the inset in panel (c) shows the PDF at smaller intensity. In panels (c) and (b), the black dash-dotted lines indicate the exponential PDF (2) and the corresponding moments (17), respectively.

statistics after sufficiently long evolution (as we explain below, at $t \gtrsim 20$ for the experiment in Fig. 1); for description of the shorter time dynamics we refer the reader to Refs. [39–44], where it was studied in more detail.

For the numerical experiment with the same initial super-Gaussian spectrum with $n = 32$ and $\alpha_0 = 64$, the ensemble-averaged kinetic energy, $\langle H_l \rangle$, potential energy, $\langle H_{nl} \rangle$, and the fourth-order moment, κ_4 , change rapidly until time $t \simeq 10$; see Fig. 2(a). Below, we call this rapid evolution the transient regime. After $t \simeq 10$, the three functions freeze, changing by less than 0.5% for $t \in [10, 1000]$. From such a behavior, one might suggest that at $t \simeq 10$ the system arrives to the statistically steady state. If this suggestion is true, then the other statistical functions must be independent of time for $t \gtrsim 10$.

In Figs. 2(b) and 2(c), we compare the ensemble-averaged moments and the PDF of intensity, additionally averaged over time intervals $t \in [20, 40]$ (shown with black in the figures), $t \in [60, 80]$ (blue), $t \in [180, 200]$ (green), and $t \in [980, 1000]$ (red). The time averaging is applied since the corresponding functions evolve slowly, and this procedure

allows us to significantly improve the accuracy of our results, most notably for measurement of the PDF; see Appendix D for details. As shown in the figures, time averaging in the intervals $t \in [20, 40]$ and $t \in [60, 80]$ gives almost identical results. However, changes start to become visible from $t \simeq 200$, when the higher order moments and the PDF at very large intensities noticeably decrease. Some moderate changes for $t \gtrsim 200$ can also be noticed for the wave-action spectrum at large wave numbers, while the autocorrelation of intensity evolves significantly at intermediate distances over the whole time interval $t \in [20, 1000]$; see Appendix C.

Hence, after the transient regime, the system arrives not to the statistically stationary state, as concluded in the previous research works, but to a *quasistationary state* (QSS). In the QSS, most of the basic statistical functions change with time very slowly, and evolution of statistics is hidden in the higher order moments, the PDF at very large intensities, the wave-action spectrum at large wave numbers, and the autocorrelation of intensity at intermediate distances.

For the experiments with wider initial spectrum (e.g., for $\alpha_0 = 16$ and 4), we observe faster convergence to the

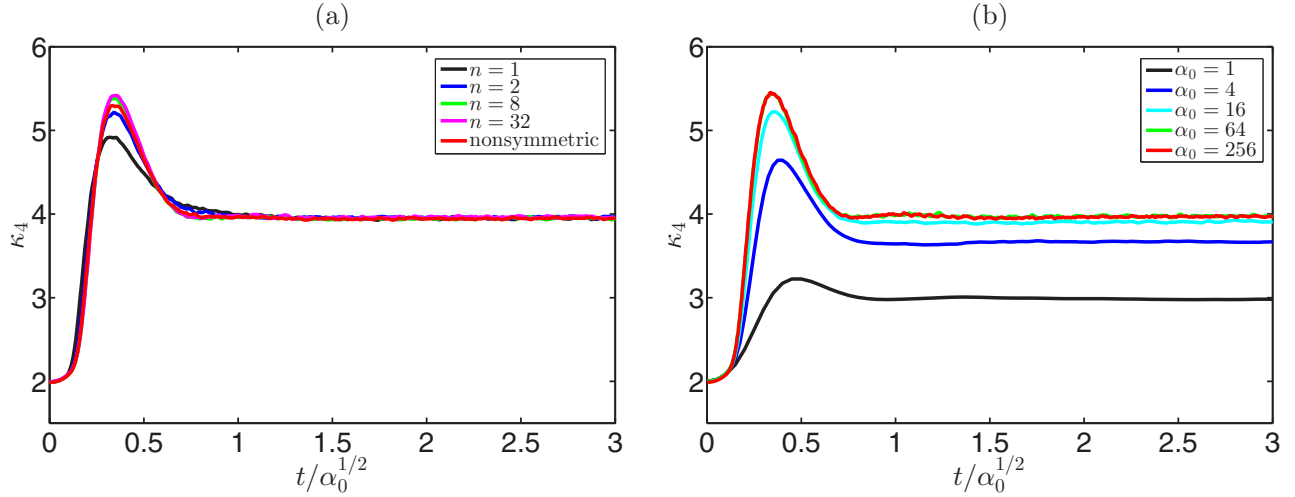


FIG. 3. The fourth-order moment κ_4 vs renormalized time $t/\sqrt{\alpha_0}$, for different numerical experiments. (a) Four simulations with nonlinearity strength $\alpha_0 = 64$ and different shapes of the initial spectrum (exponential $n = 1$, Gaussian $n = 2$, and super-Gaussian $n = 8$ and $n = 32$), and also one simulation with nonsymmetric initial spectrum of nonlinearity $\alpha_0 \approx 65.2$; see Appendix B. (b) Five simulations with different nonlinearity levels $\alpha_0 = 1, 4, 16, 64$, and 256 ; the shape of the initial spectrum is super-Gaussian with the exponent $n = 32$.

statistically steady state. For this reason, we believe that the steady state exists for the experiments with narrower initial spectrum (e.g., for $\alpha_0 = 64$ and 256) as well, but the evolution toward it takes much longer.

Qualitatively the same scenario—relatively short transient regime followed by the long QSS—is observed for other numerical experiments with different initial spectra. Quantitatively, the transient regime is significantly affected by the profile and the width of the initial spectrum. This can be seen from evolution of the fourth-order moment κ_4 versus renormalized time $t/\sqrt{\alpha_0}$, shown in the following:

- (1) Fig. 3(a) for five experiments with fixed width $\delta k = 1/\sqrt{\alpha_0}$ and different profiles of the initial spectrum (including the nonsymmetric spectrum constructed in Appendix B) and
- (2) Fig. 3(b) for five experiments with different widths $\delta k = 1/\sqrt{\alpha_0}$ and fixed profile of the initial spectrum.

Note that evolution of the ensemble-averaged kinetic and potential energies is defined uniquely from that of the fourth-order moment, as $\langle H_{nl} \rangle = -\kappa_4/2$ and $\langle H_l \rangle = -1 + 1/\alpha_0 - \langle H_{nl} \rangle$. As follows from the figures, the duration of the transient regime δT_{tr} is roughly equal to the square root of the initial nonlinearity, $\delta T_{tr} \simeq \sqrt{\alpha_0}$, and, during the transient, the fourth-order moment κ_4 takes different maximum values at slightly different renormalized times around $t/\sqrt{\alpha_0} = 0.35$ (compare with Ref. [42]), depending on the shape and width of the initial spectrum.

From these results, we can conclude that, while the duration of the transient regime increases with α_0 , the subsequent QSS lasts much longer than the transient before the final arrival to the statistically steady state. This means that, in the case of very narrow initial spectrum, it is very difficult to reach the stationary state, both using the direct numerical simulations (DNS) and an experiment in a real physical system. Indeed, examination of the stationary state with the DNS is difficult because, with decreasing spectral width δk , both the grid size and the duration $\delta T_{tr} \simeq \sqrt{\alpha_0} = 1/\delta k$ of the transient regime increase; and then the QSS takes a very long time as

well. The increase in the grid size comes from proportional elongation of the simulation box L , since the initial spectrum must be appropriately resolved; see Eqs. (21) and (22). As for an experiment, the accumulated effects of the higher order interactions over the long evolution should strongly affect the stationary state's statistics. For these reasons, in the present paper we concentrate on detailed examination of statistics in the beginning of the QSS, which we perform in the next section.

Note also that, in the QSS, the fourth-order moment κ_4 has two important properties: (i) it virtually does not change with time [see Fig. 2(a)] and (ii) its value monotonically increases with α_0 but remains bounded from above, practically reaching the upper bound $\kappa_4 = 4$ for sufficiently small initial spectral width $\alpha_0 \geq 16$ [see Figs. 3 and also Fig. 5, which we discuss in detail in the next section]. The latter means that the studied regime of narrow initial spectrum leads to the strongest deviation from Gaussianity and to the highest probability of rogue wave events possible for the PCW initial conditions. The practical independence of κ_4 on time in the QSS allows us to suggest that the asymptotic stationary value of the fourth-order moment $\kappa_{4\infty}$ should also be very close to 4 for sufficiently small initial spectral width. This determines the (asymptotic) ensemble-averaged potential energy, $\langle H_{nl} \rangle_\infty = -\kappa_{4\infty}/2 \approx -2$, as well as the kinetic one, $\langle H_l \rangle_\infty = -1 + 1/\alpha_0 - \langle H_{nl} \rangle_\infty \approx 1$. Thus, the ratio of the potential energy to the kinetic one (the stationary nonlinearity strength) α_∞ should be close to 2 [see, e.g., Fig. 2(a)], the same as for the asymptotic stationary state of the noise-induced MI [25].

V. STATISTICS OF THE QUASISTATIONARY STATE

A. The moments and the PDF

In this subsection, we perform two sets of numerical experiments. In the first set, we fix the initial nonlinearity α_0 and consider different profiles of the initial spectrum. In the second set, we fix the profile of the initial spectrum and

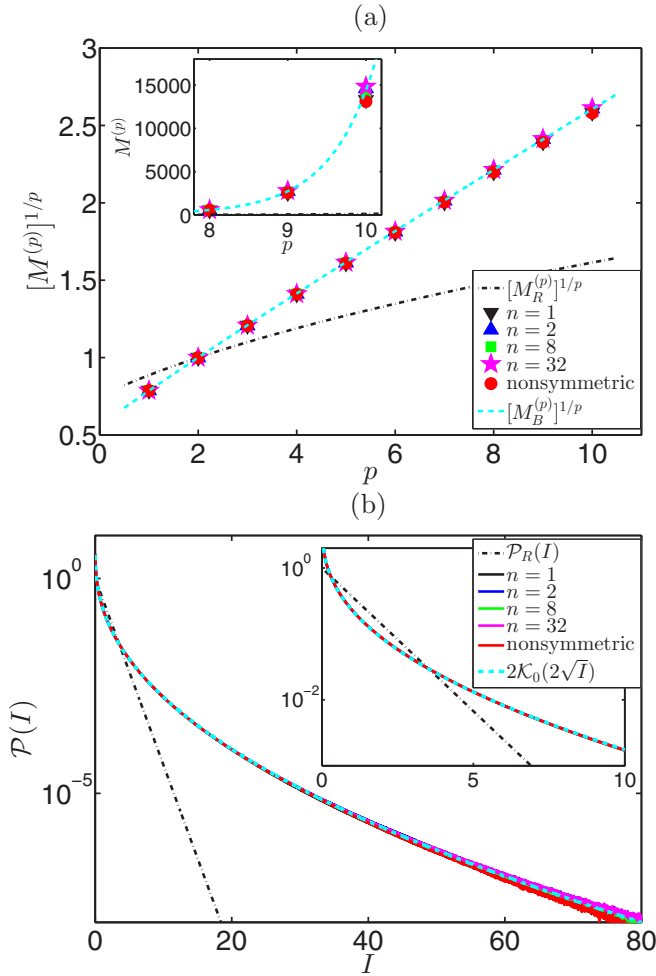


FIG. 4. Ensemble- and time-averaged statistical functions in the beginning of the QSS for four super-Gaussian initial spectra with exponents $n = 1, 2, 8, 32$ and one nonsymmetric initial spectrum: (a) the moments $[M^{(p)}]^{1/p}$ and (b) the PDF $\mathcal{P}(I)$. The initial nonlinearity is $\alpha_0 = 64$ for the four super-Gaussian spectra and $\alpha_0 \approx 65.2$ for the nonsymmetric spectrum; see Appendix B. The inset in panel (a) shows the higher order moments $M^{(p)}$ (without the $1/p$ power), and in panel (b) shows the PDF at smaller intensity. The black dash-dotted lines indicate the exponential PDF (2) and the corresponding moments (17), while the cyan dashed lines indicate the Bessel PDF (24) and the corresponding moments (25).

study different levels of α_0 . As in the previous section, in addition to ensemble averaging over random realizations of the initial conditions, we also perform time averaging over relatively short time interval $t \in [t_s, t_e]$ placed in the beginning of the QSS. The start of the interval is determined as $t_s/\sqrt{\alpha_0} = 2.5$ in order to avoid the residual small oscillations of the fourth-order moment κ_4 visible for some experiments in Fig. 3(b). The duration of the interval is set the same for all experiments, $t_e - t_s = 20$. We focus on examination of the ensemble-averaged kinetic and potential energies, the moments, and the PDF, which change very slowly during the QSS; the results for the wave-action spectrum and the autocorrelation of intensity are provided in Appendix C.

Figures 3(a) and 4 demonstrate statistical characteristics for fixed initial nonlinearity strength $\alpha_0 = 64$ and different

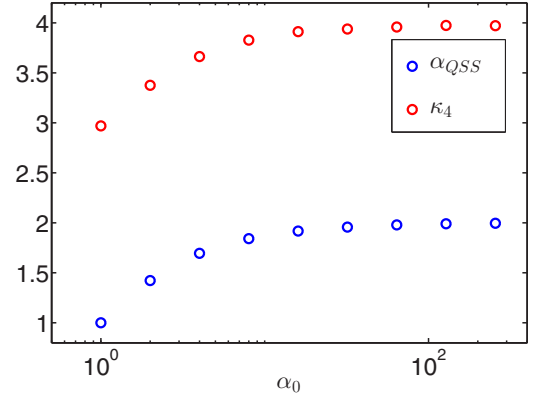


FIG. 5. The potential-to-kinetic energy ratio (the nonlinearity strength) $\alpha_{QSS} = |\langle H_{nl} \rangle|/\langle H_l \rangle$ (blue) and the fourth-order moment κ_4 (red) in the beginning of the QSS vs the initial nonlinearity α_0 , for nine experiments with super-Gaussian initial spectrum with the exponent $n = 32$ and nonlinearity levels from $\alpha_0 = 1$ to 256. Note the logarithmic horizontal scale.

profiles of the initial Fourier spectrum. As shown in the figures, in the beginning of the QSS, the presented statistics practically does not depend on the profile of the initial spectrum, even when the latter is rather arbitrary and nonsymmetric. In particular, the fourth-order moment κ_4 is very close to 4, Fig. 3(a), and the moments $[M^{(p)}]^{1/p}$ increase with p close to linearly, Fig. 4(a), exceeding significantly at large p the moments (17) corresponding to the exponential PDF (2). The PDF is slightly smaller than the exponential distribution (2) at moderate intensities $I \simeq 2$ and exceeds it by orders of magnitude at large intensities $I \gtrsim 5$, Fig. 4(b).

Note that we observe small deviations within 10% for the absolute value of the tenth-order moment $M^{(10)}$; see the inset in Fig. 4(a). However, we find difference of the same order for $M^{(10)}$ when we repeat a numerical experiment for the second time—that is, keeping the initial spectrum $A_k^{(0)}$ the same in Eq. (18), but using a different random ensemble of the initial Fourier phases ϕ_k . Additionally, the moments are directly connected to the PDF of intensity, and the difference in the latter in Fig. 4(b) is very small. For these reasons, we think that deviations of the higher order moments seen in the inset of Fig. 4(a) come mainly from finiteness and randomness of the ensemble of initial conditions and should diminish with increase of the ensemble size. We disregard such deviations here, as well as below in similar cases.

The shape of the initial spectrum does not influence visibly the wave-action spectrum in the QSS, while leading to noticeably different autocorrelation of intensity at intermediate distances; see Appendix C. Also, we have checked that other realizations of generic nonsymmetric initial spectra, characterized by the same value of α_0 , provide the same results for the moments, the PDF, and the wave-action spectrum, while leading to noticeable difference in the autocorrelation of intensity at intermediate distances.

We have repeated the described set of experiments fixing α_0 to other sufficiently large values and came to qualitatively the same results. This means, in particular, that in the beginning of the QSS the ensemble-averaged kinetic energy $\langle H_l \rangle$,

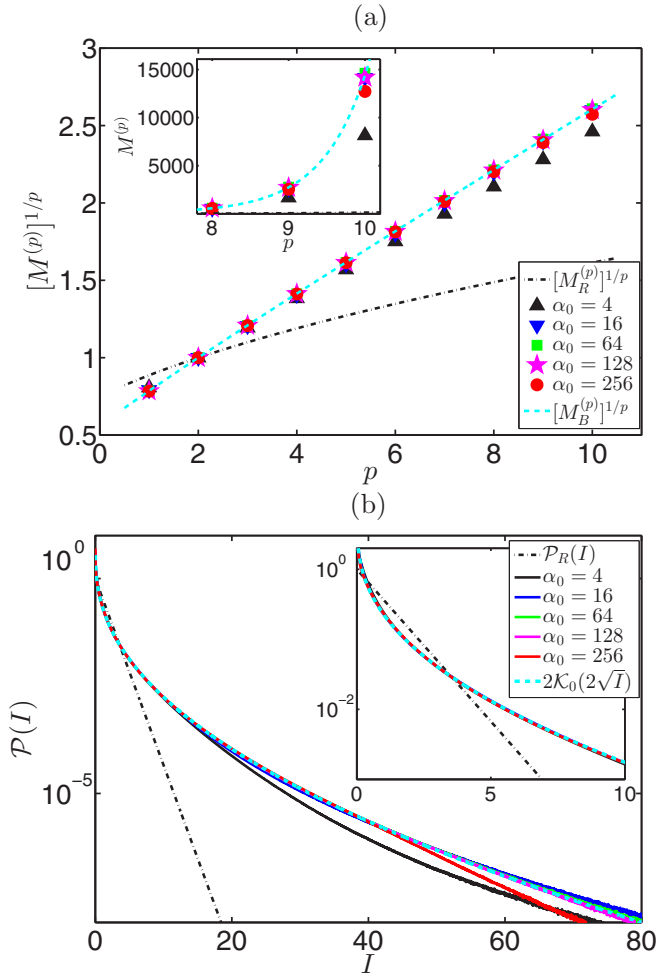


FIG. 6. Ensemble- and time-averaged statistical functions in the beginning of the QSS for different initial nonlinearity levels $\alpha_0 = 4, 16, 64, 128$, and 256 : (a) the moments $[M^{(p)}]^{1/p}$ and (b) the PDF $\mathcal{P}(I)$. The initial spectrum is super-Gaussian with the exponent $n = 32$. The inset in panel (a) shows the higher order moments $M^{(p)}$ (without the $1/p$ power) and in panel (b) shows the PDF at smaller intensity. The black dash-dotted lines indicate the exponential PDF (2) and the corresponding moments (17), while the cyan dashed lines indicate the Bessel PDF (24) and the corresponding moments (25).

potential energy $\langle H_{nl} \rangle$, and the fourth-order moment κ_4 do not depend on the shape of the initial spectrum if α_0 is sufficiently large.

In the second set of numerical experiments, we keep the shape of the initial spectrum fixed to super-Gaussian with the exponent $n = 32$, and now change the nonlinearity strength α_0 ; see Figs. 3(b), 5, and 6. The value of the fourth-order moment κ_4 in the QSS increases monotonically with α_0 , from approximately 3 for $\alpha_0 = 1$ to very close to 4 for $\alpha_0 \geq 16$; see Figs. 3(b) and 5. The potential-to-kinetic energy ratio (the nonlinearity strength in the QSS) $\alpha_{QSS} = |\langle H_{nl} \rangle| / \langle H_l \rangle$ also increases monotonically from 1 for $\alpha_0 = 1$ to very close to 2 for $\alpha_0 \geq 16$; see Fig. 5. Note that equality $\alpha_{QSS} = 1$ for $\alpha_0 = 1$ follows from conservation of the total energy. Thus, for the PCW initial conditions, the two characteristics of the QSS—the fourth-order moment and the nonlinearity

strength—are bounded from above, $\kappa_4 \leq 4$ and $\alpha_{QSS} \leq 2$, approaching to these bounds for high initial nonlinearity (small spectral width). These results could be relevant, in particular, for better understanding of random sea states [45,46].

As discussed in Sec. IV, the kinetic and potential energies, as well as the fourth-order moment, practically do not change during the QSS, so that we may suggest that in the asymptotic *stationary* state these functions have the same properties. Hence, in the long-time evolution, the studied scenario of small spectral width $\alpha_0 \gg 1$ should lead to the highest frequency of rogue waves and the strongest deviation from Gaussianity.

The moments $[M^{(p)}]^{1/p}$ turn out to be practically a universal function increasing almost linearly with p for nonlinearities $16 \leq \alpha_0 \leq 128$; see Fig. 6(a). When the initial nonlinearity is not large enough, $\alpha_0 \leq 4$, the higher order moments are noticeably smaller than this function. For the largest nonlinearity strength $\alpha_0 = 256$ that we study in the present paper, we also detect slightly smaller values for the higher order moments. In particular, the tenth-order moment $M^{(10)}$ is more than 40% smaller for $\alpha_0 = 4$ and about 10% smaller for $\alpha_0 = 256$ than that for $16 \leq \alpha_0 \leq 128$, as shown in the inset of Fig. 6(a).

The PDF for $16 \leq \alpha_0 \leq 128$ turns out to be practically a universal function as well, which exceeds the exponential distribution (2) by orders of magnitude at large intensities $I \gtrsim 5$; see Fig. 6(b). For smaller $\alpha_0 \leq 4$ and larger $\alpha_0 \geq 256$ initial nonlinearities, we observe the PDF to be slightly smaller at large intensities, with deviations by less than one order of magnitude within the interval $I \in [20, 80]$. These deviations explain the smaller values for the higher order moments compared to $16 \leq \alpha_0 \leq 128$, and we will address them in more detail in the next paragraphs.

Note that the PDFs similar in shape but with lower tails were obtained in Ref. [34] for the largest optical power and in Refs. [32,33] for the initial conditions with the largest fraction of PCW and the largest correlation length.

The wave-action spectrum depends significantly on α_0 , which is most noticeable at small wave numbers, and the autocorrelation of intensity changes strongly with α_0 at intermediate distances; see Appendix C.

B. Insights from wave-field dynamics

The deviations of the PDF for $\alpha_0 \leq 4$ and $\alpha_0 \geq 256$ from almost a universal function at $16 \leq \alpha_0 \leq 128$ can be understood qualitatively by looking at the wave-field dynamics. Each realization of the initial conditions represents a collection of humps of characteristic width $\delta x \simeq \sqrt{\alpha_0}$, and the smaller scale breather-like structures of width $\simeq 1$ gradually emerge on each hump at the early stage of motion; see, e.g., Fig. 1 and Refs. [39–44]. To observe evolution of the humps, we can remove the smaller scale oscillations associated with the breather-like structures by applying a filter in space of moving average type to the wave-field intensity.

Figure 7 demonstrates results of such a smoothing performed with the weighted local regression (lowess) filter [47] over the spatial window $\ell = 4\pi$, together with the nonsmoothed intensity and the initial intensity, for one realization of the initial conditions with nonlinearity $\alpha_0 = 64$ in Fig. 7(a)

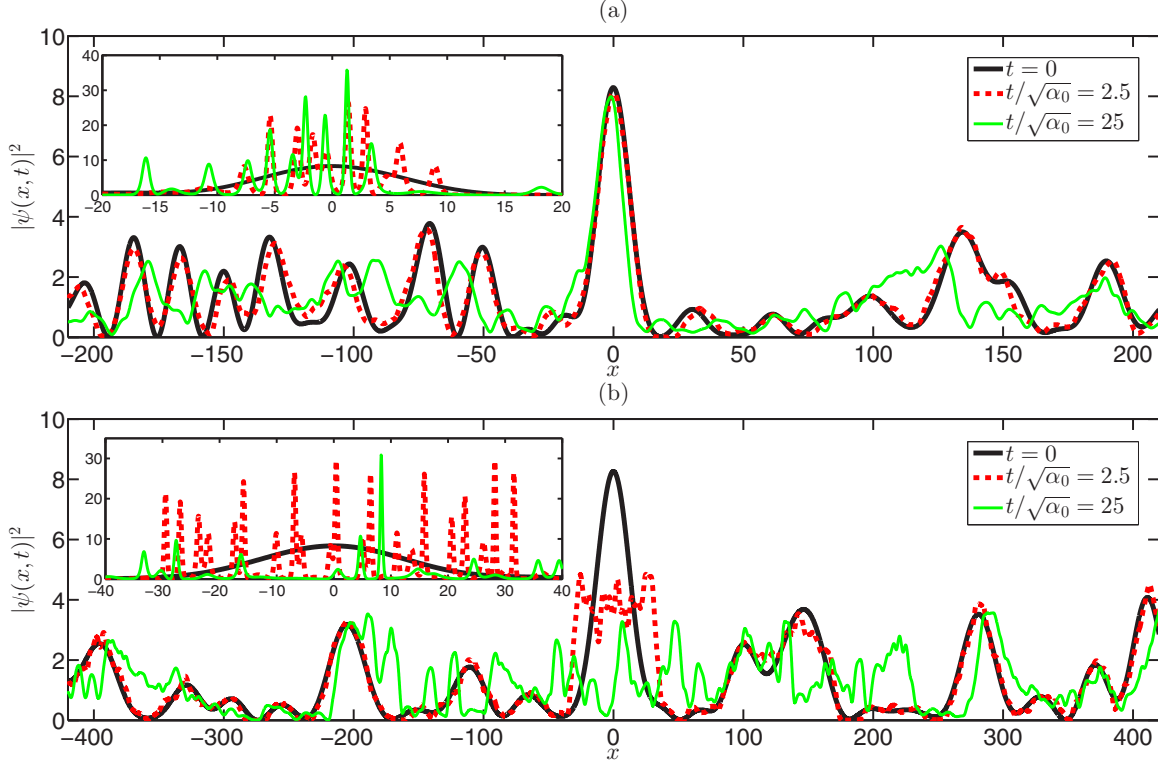


FIG. 7. Smoothed intensity $|\psi|^2$ vs spatial coordinate x at different times for one realization of a PCW, for the initial nonlinearity (a) $\alpha_0 = 64$ (the same realization as in Fig. 1) and (b) $\alpha_0 = 256$; the initial spectrum is super-Gaussian with the exponent $n = 32$. The black lines indicate the initial (nonsmoothed) intensity at $t = 0$; the dashed red and thin green lines show the smoothed intensity at renormalized times $t/\sqrt{\alpha_0} = 2.5$ and $t/\sqrt{\alpha_0} = 25$, respectively. The time $t/\sqrt{\alpha_0} = 2.5$ corresponds to the beginning of the QSS. The spatial smoothing is performed with the weighted local regression (lowess) filter over the window $\ell = 4\pi$. The insets show the original (nonsmoothed) intensity at the same times on the scale of the largest hump; note the different vertical scales compared to the main figures. The maximum of the initial amplitude is shifted to $x = 0$ for better visualization.

and $\alpha_0 = 256$ in Fig. 7(b). Note that, as we have checked, the smoothing windows from $\ell = \pi$ to 8π provide qualitatively the same results. The smoothed intensity is shown in the figures at two different times $t/\sqrt{\alpha_0} = 2.5$ and $t/\sqrt{\alpha_0} = 25$, the first of which corresponds to the beginning of the QSS; the insets of the figures show the original (nonsmoothed) intensity at the same times on the scale of the largest hump.

For the first experiment with $\alpha_0 = 64$, one can see that, while the original (nonsmoothed) intensity in the beginning of the QSS may exceed the maximum of the initial intensity by more than three times due to emergence of the smaller scale breather-like structures, the smoothed intensity at the same time practically coincides with the initial one, Fig. 7(a). During the subsequent evolution, the humps revealed by the smoothing procedure gradually mix with each other and disappear, though this turns out to be a long process. In particular, the largest hump with maximum intensity $|\psi|^2 \simeq 8$ survives and retains its shape even at $t/\sqrt{\alpha_0} = 25$, which corresponds to $t = 200$, i.e., the time-averaging interval $t \in [180, 200]$ shown in Figs. 2(b) and 2(c) with the green color. Qualitatively the same scenario is observed for other realizations of the initial conditions with initial nonlinearity from $\alpha_0 = 16$ to 128.

The above observations allow to suggest the analytical form of the universal PDF for $16 \leq \alpha_0 \leq 128$. Indeed, in the QSS, the smoothed intensity I_s evolves slowly, and in the

beginning of this state it practically coincides with the initial intensity. The initial intensity is exponentially distributed, so that in the beginning of the QSS the smoothed intensity is exponentially distributed too, $\mathcal{P}_s(I_s) = \exp(-I_s)$. Let us consider a sufficiently small element of a hump with smoothed intensity I_s . This element provides a contribution $\mathcal{P}_e(I | I_s)$ to the overall PDF of intensity $I = |\psi|^2$ (nonsmoothed), depending on the smaller scale breather-like structures evolving on its background. Assuming the simplest scenario that each such contribution is exponential distribution with mean intensity I_s , i.e., $\mathcal{P}_e(I | I_s) = I_s^{-1} \exp(-I/I_s)$, where the prefactor I_s^{-1} comes from normalization condition, we come to the following estimate for the overall PDF,

$$\begin{aligned} \mathcal{P}_B(I) &= \int_0^{+\infty} \mathcal{P}_e(I | I_s) \times \mathcal{P}_s(I_s) dI_s \\ &= \int_0^{+\infty} I_s^{-1} e^{-I/I_s} dI_s = 2\mathcal{K}_0(2\sqrt{I}), \end{aligned} \quad (24)$$

where \mathcal{K}_0 denotes the modified Bessel function of the second kind of zeroth order. The estimate (24) is shown in Figs. 4(b) and 6(b) with the dashed cyan lines, and for the initial nonlinearities $16 \leq \alpha_0 \leq 128$ it is in a remarkable agreement with numerical simulations.

The Bessel PDF (24) represents a strongly nonexponential distribution, which decays at large intensity as

$$\mathcal{P}_B(I) \rightarrow \frac{\sqrt{\pi}}{I^{1/4}} e^{-2\sqrt{I}} \quad \text{for } I \rightarrow +\infty,$$

and corresponds to the moments

$$M_B^{(p)} = \int_0^{+\infty} |\psi|^p \mathcal{P}_B(|\psi|^2) d|\psi|^2 = \Gamma_{1+p/2}^2, \quad (25)$$

in particular, the fourth-order moment $\kappa_4 = 4$. Note that, quite remarkably, the latter values equal the squares of the moments (17) corresponding to the exponential PDF (2). The moments following from the Bessel PDF are in very good agreement with those observed numerically in the beginning of the QSS, as can be seen in Figs. 4(a) and 6(a) for $16 \leq \alpha_0 \leq 128$. Then, the close to linear dependency of $[M^{(p)}]^{1/p}$ with p can be explained by the asymptotic expansion of the Gamma function $\Gamma_{1+z} \sim \sqrt{2\pi z} (\frac{z}{e})^z$ at $z \rightarrow +\infty$ (the Stirling's formula) applied to Eq. (25),

$$[M_B^{(p)}]^{1/p} \sim (\pi p)^{1/p} \cdot \frac{p}{2e} \quad \text{as } p \rightarrow +\infty. \quad (26)$$

For the experiment shown in Fig. 7(b) with initial nonlinearity $\alpha_0 = 256$, the behavior of the smoothed intensity has a significant difference. The largest hump in this case substantially decreases in intensity and broadens already to the beginning of the QSS, and then splits to several smaller humps: Compare the smoothed intensities at $t/\sqrt{\alpha_0} = 2.5$ ($t = 40$) for Fig. 7(b) and at $t/\sqrt{\alpha_0} = 25$ ($t = 200$) for Fig. 7(a). Note that this process can be seen even by looking at the original (nonsmoothed) intensity, as indicated in the inset of Fig. 7(b). The smaller humps, however, may preserve their shape for a sufficiently long time. We think that the splitting of the largest humps, which are the background for evolving on them smaller scale breather-like structures, is the reason why the PDF for $\alpha_0 = 256$ is slightly smaller at very large intensities $I \gtrsim 50$ than the PDF given by the estimate (24).

Performing experiments with individual realizations characterized by even larger initial nonlinearity $\alpha_0 > 256$, we observe that, in the beginning of the QSS, the tendency for splitting of the humps depends on the humps' width and maximum intensity. Specifically, for fixed width (which is proportional to $\sqrt{\alpha_0}$), humps with maximum intensity larger than some threshold tend to substantially decrease in intensity and broaden, and then split to smaller humps, while the initially smaller humps may survive for a long time. The value of the intensity threshold, dividing the different behavior, decreases with increasing α_0 . Hence, we expect that, for larger nonlinearity $\alpha_0 > 256$, the tail of the PDF should deviate from the Bessel estimate (24) to lower values even more pronouncedly and starting from smaller intensities. This should result in the higher order moments smaller than the estimate (25) too, with deviation increasing with α_0 .

Similarly, we may assume that for $16 \leq \alpha_0 \leq 128$ the PDF and the moments should also deviate from the estimates (24) and (25), but these deviations should be noticeable from so large intensities I , which we do not observe in our limited numerical experiments. Note that a visible deviation of the PDF from the Bessel estimate (24), that starts from very large intensities, may lead to very small corrections of the higher

order moments, compare the results for $\alpha_0 = 256$ in Figs. 6(b) and 6(a), because the remaining part of the integral at these intensities is very small; see, e.g., Eqs. (17) and (25).

Note also that, when the initial nonlinearity is not large enough, $\alpha_0 \leq 4$, the humps have characteristic width of unity order, $\delta x \lesssim 2$. Then, decomposition of evolution by that of the humps and of the breather-like structures should be inapplicable, as the latter have width of unity order too, and it is natural to expect the PDF deviating from the Bessel estimate (24). We indeed observe this deviation in the numerical simulations, as demonstrated in Fig. 6(b).

The probability to meet intensity above the rogue wave threshold $I > 8$ (see, e.g., Refs. [1–3]) can be calculated as the corresponding integral of the PDF,

$$P_{RW} = \int_8^{+\infty} \mathcal{P}(I) dI, \quad (27)$$

and for the PDF (24) the result is $P_{RW} = 1.1 \times 10^{-2}$. To our knowledge, this is the largest probability of rogue waves that has been reached so far for (quasi)stationary states of the 1D-NLSE developing from various types of initial conditions. For instance, the corresponding probability for the exponential PDF (2) is 3.4×10^{-4} , which is smaller by 1.5 orders of magnitude. For the numerical experiments with $\alpha_0 \geq 16$, we measure the same result $P_{RW} = 1.1 \times 10^{-2}$ as for the Bessel PDF, while for smaller nonlinearities $\alpha_0 = 4$ and $\alpha_0 = 1$ we find $P_{RW} = 10^{-2}$ and $P_{RW} = 6.1 \times 10^{-3}$, respectively. Note that for $\alpha_0 = 256$ we measure practically the same probability P_{RW} as for $16 \leq \alpha_0 \leq 128$; this happens because the PDF for $\alpha_0 = 256$ deviates from the Bessel fit starting from very large intensities $I \gtrsim 50$, where the remaining part of the integral (27) is very small.

Summarizing the experiments shown in Fig. 7, we conclude that, in the QSS, evolution of the wave field can be subdivided by the fast changes with time of the smaller scale breather-like structures moving on background of the humps and the slow motion of the humps. For initial nonlinearities $16 \leq \alpha_0 \leq 128$, all humps which we observe in our numerical simulations evolve slowly. For larger values $\alpha_0 \geq 256$, the largest humps tend to significantly decrease in intensity and broaden at the beginning of the QSS, and then split to smaller humps, while the initially smaller humps survive and retain their shape for a long time.

We think that the slow evolution of the humps is the main process that underlies the QSS and determines the slow changes with time of its basic statistical functions. If this suggestion is true, then we can guess that in the asymptotic *stationary* state all humps should disappear, so that the smoothed intensity should everywhere be sufficiently close to unity and the tail of the PDF should be significantly lower than for the Bessel PDF (24).

As for a general examination of possible causes that might lead to the different behavior of the largest humps for $\alpha_0 \geq 256$, we leave it to future studies.

C. Rogue waves

Figure 8 shows the largest rogue wave event detected in the beginning of the QSS for the experiment with super-Gaussian initial spectrum with the exponent $n = 32$ and nonlinearity

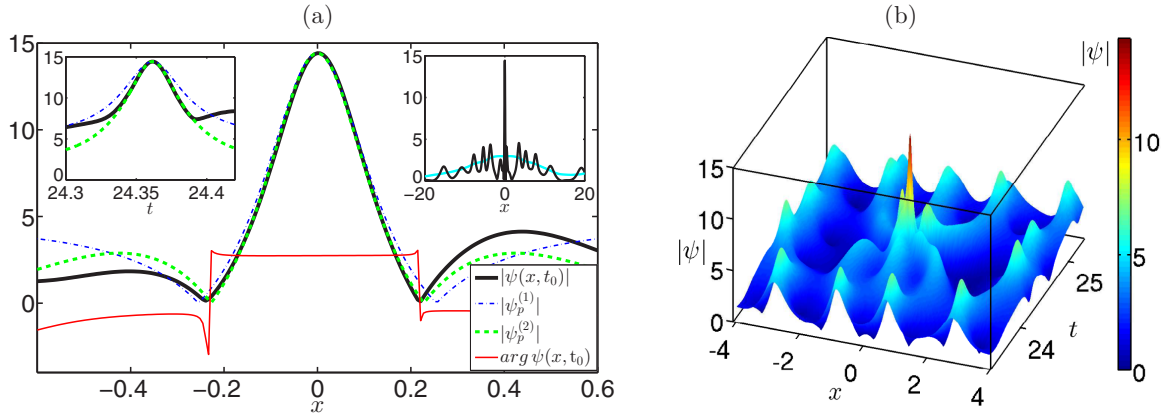


FIG. 8. The largest rogue wave detected in the beginning of the QSS for the ensemble with super-Gaussian initial spectrum with the exponent $n = 32$ and nonlinearity strength $\alpha_0 = 64$; the maximum amplitude is shifted to $x = 0$ for better visualization. (a) The thick black and the thin red lines show the coordinate dependencies for the amplitude $|\psi|$ and the phase $\arg \psi$, while the dash-dotted blue and the dashed green indicate fits by the rational breather solutions of the first and second orders. The left inset demonstrates time dependency for the maximum amplitude $\max_x |\psi|$ (thick black) and its fits with the corresponding rational breather solutions (dash-dotted blue and dashed green), while the right inset shows the amplitude $|\psi|$ (black) and the smoothed amplitude (cyan) in the x space at the time of the maximum elevation. The smoothing is performed with the lowess filter over the window $\ell = 4\pi$. (b) Space-time representation of the amplitude $|\psi(x, t)|$ near the rogue wave event.

strength $\alpha_0 = 64$. This event occurred at time $t_0 \approx 24.36$, had duration $\Delta T \simeq 0.07$, and reached maximum amplitude $\max |\psi| \approx 14.4$ corresponding to intensity $I \approx 207$.

The rogue wave emerged on background of the hump having maximum amplitude close to 3 and exceeded the latter by about five times; see the right inset in Fig. 8(a). We observe such behavior for other rogue waves as well: The initial conditions contain large humps exceeding the average amplitude by several times, and evolution of the smaller scale breather-like structures on background of these humps leads to spikes exceeding amplitude of the humps by several times. This implies that rogue waves tend to appear in regions occupied by large humps, similar to emergence of rogue waves on caustics in multidimensional spatial systems [48,49].

We routinely detect rogue waves with maximum amplitude 10 times larger than the average one, $\max |\psi| > 10$. For instance, among 20 largest rogue waves emerged from the same ensemble of initial conditions, all 20 have maximum amplitude exceeding 10.

The spatial profile $|\psi(x, t_0)|$ of the rogue wave in Fig. 8(a) at the time of the maximal elevation t_0 , as well as the temporal evolution of the maximum amplitude $\max_x |\psi|$, are very well approximated by the amplitude-scaled rational breather solution of the second order, as indicated by the dashed green lines in the figure and the left inset. The rational breather solution of the first order, also known as the Peregrine breather [5], is localized in space and time rational solution of the 1D-NLSE (1),

$$\psi_p^{(1)}(x, t) = e^{it} \left[1 - \frac{4(1 + 2it)}{1 + 2x^2 + 4t^2} \right]. \quad (28)$$

The next-order rational breathers are too cumbersome, and we refer the reader to Ref. [7]. If $\psi_p(x, t)$ is a solution of the 1D-NLSE, then $A_0 \psi_p(\varkappa, \sigma)$, where $\varkappa = |A_0|(x - x_0)$ and $\sigma = |A_0|^2(t - t_0)$, is also a solution. In Fig. 8(a), the rational breathers of the first (dash-dotted blue) and the second (dashed

green) orders are scaled with parameters A_0 , x_0 , and t_0 to fit the observed rogue wave in its maximum amplitude, position, and time of occurrence. Note that the phase of the rogue wave $\arg \psi(x, t_0)$ is almost constant near the amplitude maximum, as in the case of the rational breathers at the time of their maximal elevation. The space-time representation of the rogue wave shown in Fig. 8(b) looks as a collision of three pulses.

For each of our numerical experiments with initial nonlinearity from $\alpha_0 = 4$ to 256 and with different profiles of the initial spectrum, including the nonsymmetric spectra, we have checked the largest 20 rogue waves detected in the beginning of the QSS. We have found that all of these rogue waves are very well approximated by the rational breather solutions of either the first (the Peregrine breather), or the second orders, with flat phase profile $\arg \psi(x, t_0) \approx \text{const}$ near the amplitude maximum.

VI. DISCUSSION AND CONCLUSIONS

We have studied statistics of waves for the integrable turbulence developing from partially coherent waves (PCW) of narrowband spectrum. As a criterion for narrowness, we have demanded the initial nonlinearity strength (i.e., the dimensionless ratio of the potential energy to the kinetic one) to be large, $\alpha_0 \gg 1$; in our dimensionless formulation, the nonlinearity strength equals to the average intensity divided by the square spectral width (3). Motivated by the previous publications [28,34] that indicated such initial conditions as promising for extreme generation of rogue waves, we have examined the basic statistical characteristics of the turbulence, focusing on the moments and the PDF of intensity, and have analyzed the emerging rogue waves.

For narrow initial spectrum $\alpha_0 \gg 1$, we have found that, after a relatively short transient regime, the system enters a state which we call quasistationary (QSS). In the QSS, most of the basic statistical functions—including the kinetic and potential

energies, the moments, and the PDF of intensity—change with time very slowly, and evolution of statistics is hidden in the higher order moments, the PDF at very large intensities, the wave-action spectrum at large wave numbers, and the autocorrelation of intensity at intermediate distances. The evolution within the QSS toward the long-term statistically stationary state turns out to be very long. To our knowledge, the existence of such a state has not been reported previously. The slow evolution of statistics in the QSS and a very distant statistically stationary state are the reasons why we believe that, for any possible practical application, examination of the QSS is important.

In the QSS, the potential-to-kinetic energy ratio (i.e., the nonlinearity strength) and the fourth-order moment increase monotonically for vanishing initial spectral width (i.e., increasing initial nonlinearity) but turn out to be bounded from above, $\alpha_{QSS} \leq 2$ and $\kappa_4 \leq 4$. Hence, by demanding narrowness of the initial spectrum, we obtain the integrable turbulence that develops with the maximum nonlinearity strength $\alpha_{QSS} \approx 2$ and the maximum fourth-order moment $\kappa_4 \approx 4$, possible for the PCW initial conditions. Equivalently, this limiting case could be reached by fixing the initial spectral width and increasing the average intensity. The kinetic and potential energies, as well as the fourth-order moment, practically do not change during the QSS, and we think that in the asymptotic *stationary* state they have the same values: $\langle H_I \rangle_\infty \approx 1$, $\langle H_{nl} \rangle_\infty \approx -2$, and $\kappa_{4\infty} \approx 4$.

In the beginning of the QSS, the PDF of intensity is slightly smaller than the exponential distribution (2) at moderate intensities $I \approx 2$, and exceeds it by orders of magnitude at large intensities $I \gtrsim 5$. The PDF does not depend on the shape of the initial spectrum and represents practically a universal function for the initial nonlinearities $16 \lesssim \alpha_0 \lesssim 128$, which is very well approximated by the Bessel function (24). The corresponding probability $P_{RW} = 1.1 \times 10^{-2}$ to meet intensity above the rogue wave threshold, $I > 8$, is higher by 1.5 orders of magnitude than for the exponential PDF (2). To our knowledge, these two results—the fourth-order moment $\kappa_4 \approx 4$ and the observed frequency of rogue waves—are the largest that have been reached so far for (quasi)stationary states of the 1D-NLSE developing from various types of initial conditions.

For the initial nonlinearity $\alpha_0 = 256$, we observe deviation of the far tail $I \gtrsim 50$ of the PDF from the universal function (24) to *lower values*; however, this deviation does not affect the probability P_{RW} visibly. From consideration of the wave-field dynamics in Sec. V, we expect that for larger initial nonlinearity $\alpha_0 > 256$ (narrower spectrum) the tail of the PDF will be even lower and the deviation will start from smaller intensities.

In our numerical experiments, we routinely detect rogue waves 10 times larger than the average amplitude. We have examined the largest rogue waves detected in the beginning of the QSS and found that all of these rogue waves are very well approximated—both in space and in time—by the rational breather solutions of either the first (the Peregrine breather) or the second orders.

Generation of a PCW of narrowband spectrum in a real physical system may be obstructed by presence of a wide-spectrum noise that may affect statistics of the developing

integrable turbulence. However, as we have checked in Appendix E, even for significant noise levels, most of the basic statistical functions in the QSS—including the potential energy, the moments, and the PDF of intensity—are practically unchanged when the noise is present.

Our main motivation for this study was the fundamental investigation of the integrable turbulence in a setting that allows very frequent appearance of rogue waves. As such, we hope that it will stimulate new experimental and theoretical research in the field of nonlinear random waves. In particular, the soliton gas theory may be promising to explain the long-time statistics in the case of narrow initial spectrum (high initial nonlinearity) and to understand the maximum value of the stationary fourth-order moment $\kappa_4 = 4$. Also, our results may be useful for practical applications as well, for instance, as a construction method for a wave field characterized by frequent spikes, exceeding the average power by several hundred times, and with nearly steady statistics during its time evolution.

ACKNOWLEDGMENTS

The authors thank A. Gelash, A. Tikan, and F. Copie for fruitful discussions. Simulations were performed at the Novosibirsk Supercomputer Center (NSU). This work has been partially supported by the Agence Nationale de la Recherche through the LABEX CEMPI Project (Project No. ANR-11-LABX-0007), the DYDICO project of the I-SITE ULNE (ANR-16-IDEX-004), and the Ministry of Higher Education and Research, Hauts-De-France Regional Council and European Regional Development Fund (ERDF) through the Contrat de Projets Etat-Region (CPER Photonics for Society Grant No. P4S). The work of D.S.A. (simulations) was supported by the state assignment of IO RAS, Grant No. 0128-2021-0003.

APPENDIX A: SCALING TRANSFORMATIONS OF THE 1D-NLSE

The problem of evolution within the focusing 1D-NLSE with arbitrary dispersion $\beta > 0$ and nonlinearity $\gamma > 0$ coefficients,

$$i\Psi_T + \beta \Psi_{XX} + \gamma |\Psi|^2 \Psi = 0,$$

that starts from initial conditions $\Psi|_{t=0} = \Psi_0$ of arbitrary average intensity, $|\Psi_0|^2 = N_0$, can be renormalized to unit dispersion and nonlinearity coefficients, and unit average intensity,

$$i\psi_t + \psi_{xx} + |\psi|^2 \psi = 0, \quad \psi|_{t=0} = \psi_0, \quad |\psi_0|^2 = 1,$$

with the help of the scaling transformations $\Psi = \sqrt{N_0} \psi$, $T = t/\gamma N_0$, and $X = x\sqrt{\beta/\gamma N_0}$. With these transformations, the wave number renormalizes as $K = k\sqrt{\gamma N_0/\beta}$. This means that the initial nonlinearity strength α_0 that is connected with the dimensionless spectral width δk as $\alpha_0 = \delta k^{-2}$ (see Sec. II) depends on the (original) spectral width $\delta K = \delta k\sqrt{\gamma N_0/\beta}$ and the average intensity $N_0 = \langle |\Psi_0|^2 \rangle$ as

$$\alpha_0 = \frac{1}{\delta k^2} \Big|_{t=0} = \frac{\gamma}{\beta} \frac{\langle |\Psi_0|^2 \rangle}{\delta K^2} \Big|_{T=0};$$

compare with Eq. (3). Hence, the nonlinearity strength can be enhanced by both increasing the average intensity N_0 and decreasing the spectral width δK . In particular, the experiments in Ref. [34] with larger initial intensities (optical power), which demonstrated the larger probability of rogue waves, are equivalent in our formulation to the smaller (renormalized) initial spectral width δk and the higher nonlinearity α_0 .

The advantage of criterion $\alpha_0 \gg 1$ for narrowness of the initial spectrum comes from dimensionless nature of the quantity α_0 , which can be computed readily using the dimensional definitions of the kinetic and potential energies,

$$H_l = \beta \overline{|\Psi_X|^2}, \quad H_{nl} = -\gamma \overline{|\Psi|^4}/2;$$

compare with Eqs. (9) and (10). For this reason, we use the nonlinearity strength α_0 as a characteristic of the spectral width, instead of setting the spectral width directly.

APPENDIX B: CONSTRUCTION OF NONSYMMETRIC INITIAL SPECTRUM

We construct generic (nonsymmetric) Fourier spectrum $A_k^{(0)}$ in Eq. (18) in the following way. At the first step, we generate an “intermediate” spectrum

$$\tilde{A}_k^{(0)} = C_0 \exp \left[f_k - (1 - h_k) \left(\frac{|k|}{\theta_l} \right)^{n_l} - h_k \left(\frac{|k|}{\theta_r} \right)^{n_r} \right], \quad (\text{B1})$$

where $f_k \approx 1$ is generic real function, h_k is the Heaviside step function, and C_0 is a constant determined from normalization condition $|\overline{\psi_0(x)}|^2 = 1$. The left and right decay exponents n_l and n_r , together with the left and right “spectral widths” θ_l and θ_r , enable the spectrum $\tilde{A}_k^{(0)}$ to decay differently in the limits $k \rightarrow -\infty$ and $k \rightarrow +\infty$. The function f_k is composed as superposition of linear waves with Gaussian spectrum and arbitrary phases, similar to how we define the initial conditions (18) and (19).

The “intermediate” spectrum has nonzero momentum

$$\sum_k k [\tilde{A}_k^{(0)}]^2 \neq 0$$

[see Eq. (7)], and to eliminate it, at the second step we construct the “final” spectrum $A_k^{(0)}$ by shifting the “intermediate” one by a constant wave number k_0 ,

$$A_k^{(0)} = \tilde{A}_{k-k_0}^{(0)}, \quad k_0 = - \sum_k k [\tilde{A}_k^{(0)}]^2. \quad (\text{B2})$$

For the function f_k , this shift is performed with (forward) Fourier transform to the x space, multiplication by $e^{-ik_0 x}$, and then (backward) Fourier transform to the k space.

One of the examples of nonsymmetric spectra $A_k^{(0)}$ used in our numerical experiments is shown in Fig. 9. It has left and right decay exponents $n_l = 2$ and $n_r = 32$ and equal left and right “spectral widths” $\theta_l = \theta_r = 0.24$, and is characterized by the ensemble-average potential-to-kinetic energy ratio (nonlinearity strength) $\alpha_0 \approx 65.2$. For our simulation parameters, in the region $[-\theta_l, \theta_r]$ this spectrum is resolved with $(\theta_l + \theta_r)/\Delta k \approx 123$ harmonics, where $\Delta k = 2\pi/L = 1/256$ is the distance between the neighbor harmonics and $L = 512\pi$ is the length of the simulation box.

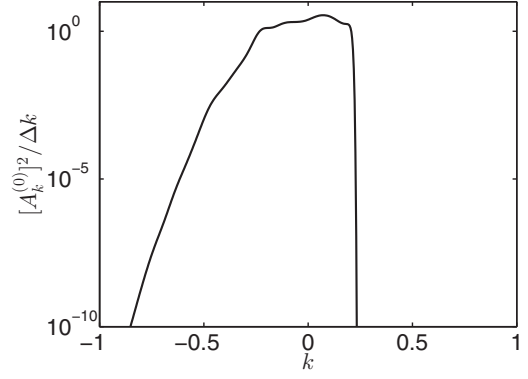


FIG. 9. Nonsymmetric initial wave-action spectrum $[A_k^{(0)}]^2/\Delta k$ for one of the numerical experiments. The spectrum has left and right decay exponents $n_l = 2$ and $n_r = 32$, and equal left and right “spectral widths” $\theta_l = \theta_r = 0.24$ [see Eqs. (B1) and (B2)] and is characterized by the ensemble-average potential-to-kinetic energy ratio (nonlinearity strength) $\alpha_0 \approx 65.2$. The modulation at small wave numbers seen in the figure comes from the function f_k in Eq. (B1).

APPENDIX C: WAVE-ACTION SPECTRUM AND AUTOCORRELATION OF INTENSITY

In the main part of the paper, we have focused on examination of the kinetic and potential energies, the moments, and the PDF of intensity. In this Appendix, we consider two other important statistical functions: the wave-action spectrum,

$$S_k(t) = \langle |\psi_k|^2 \rangle / \Delta k, \quad (\text{C1})$$

where $\Delta k = 2\pi/L$ is distance between the neighbor harmonics, and the autocorrelation of intensity,

$$g_2(x, t) = \frac{\overline{\langle |\psi(y+x, t)|^2 |\psi(y, t)|^2 \rangle}}{\langle |\psi(y, t)|^2 \rangle^2}. \quad (\text{C2})$$

In the latter relation, the overline means spatial averaging over the y coordinate. Note that at $x = 0$ the autocorrelation equals to the fourth-order moment, $g_2(0, t) = \kappa_4(t)$, and at $x \rightarrow \infty$ it must approach unity, $g_2(x, t) \rightarrow 1$. For the wave-action spectrum, we use normalization $\int S_k dk = \langle |\psi|^2 \rangle = 1$.

1. Time evolution

First, we compare the ensemble-averaged statistical functions, additionally averaged over time intervals $t \in [20, 40]$ (shown with black in Fig. 10), $t \in [60, 80]$ (blue), $t \in [180, 200]$ (green), and $t \in [980, 1000]$ (red); concerning the time averaging, see Appendix D below.

For the wave-action spectrum, time averaging in the intervals $t \in [20, 40]$ and $t \in [60, 80]$ gives almost identical results [Fig. 10(a)]. However, starting from $t \simeq 200$, the triangular shape of the wave-action spectrum at small wave numbers $|k| \lesssim 1$ becomes less sharp, and at large wave numbers $|k| \gtrsim 10$ the spectrum significantly decreases.

In contrast to the wave-action spectrum, the autocorrelation of intensity changes pronouncedly over the whole time interval $t \in [20, 1000]$, as shown in Fig. 10(b). Its significant evolution with time is observed at intermediate distances $1 \lesssim |x| \lesssim 20$ between the steady bell-shaped central peak of

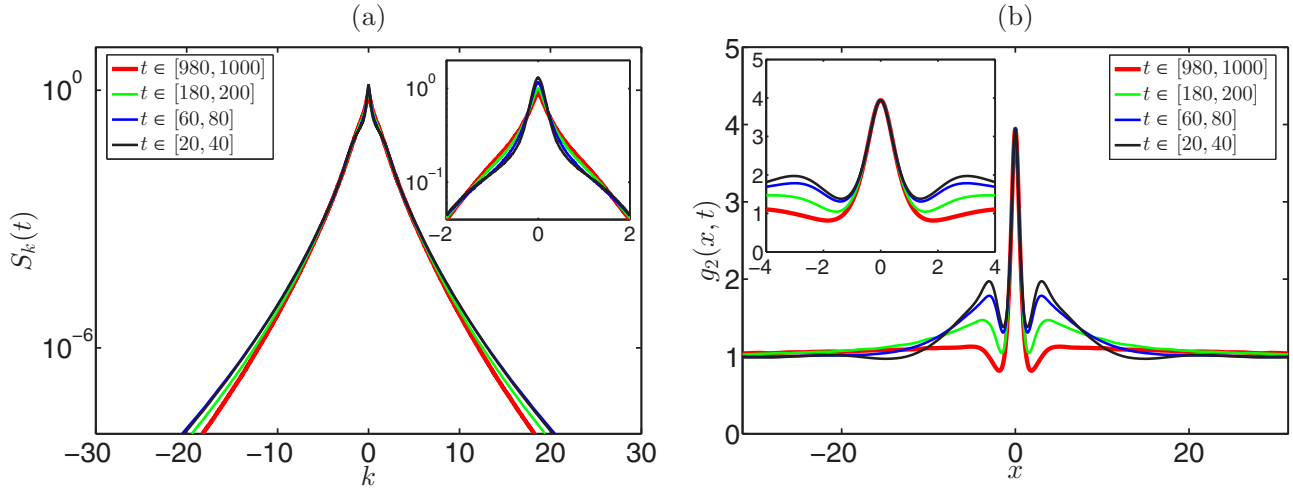


FIG. 10. Averaged over ensemble and different time intervals statistical functions: (a) the wave-action spectrum S_k and (b) the autocorrelation of intensity $g_2(x)$. The initial spectrum is super-Gaussian with the exponent $n = 32$ and nonlinearity strength $\alpha_0 = 64$. The insets show the same functions as in the main figures with smaller scales.

full width at half maximum $\Delta_{FWHM} \simeq 1.4$ and large distances $|x| \gtrsim 20$ where the autocorrelation reaches unity. Note that the distance where the autocorrelation practically reaches unity shrinks from $|x| \simeq 20$ at $t \simeq 40$ to $|x| \simeq 4$ at $t \simeq 1000$.

2. Statistics of the quasistationary state

Following the main part of the paper, we consider two sets of numerical experiments. In the first set, we fix the initial nonlinearity strength to $\alpha_0 = 64$ and consider different profiles of the initial spectrum; the results of these experiments are shown in Fig. 11. In the second set, we fix the shape of the initial spectrum to super-Gaussian with the exponent $n = 32$ and study different levels of α_0 ; see Fig. 12. In addition to ensemble-averaging over random realizations of the initial conditions, we also perform time averaging over relatively short time interval $t \in [t_s, t_e]$ placed in the

beginning of the QSS. The start of the interval is determined as $t_s/\sqrt{\alpha_0} = 2.5$ and its duration is set the same for all experiments, $t_e - t_s = 20$.

As shown in Fig. 11(a), the wave-action spectrum in the beginning of the QSS practically does not depend on the profile of the initial spectrum, even when the latter is rather arbitrary and nonsymmetric. In the QSS, the wave-action spectrum turns out to be symmetric, decays slightly slower than exponential at large wave numbers $|k| \gtrsim 4$, and has a sharp triangular shape at small wave numbers $|k| \lesssim 1$.

The autocorrelation of intensity, in contrast, depends on shape of the initial spectrum noticeably, and this dependency is observed at intermediate distances $2 \lesssim |x| \lesssim 20$ [Fig. 11(b)] between the universal central peak of full width at half maximum $\Delta_{FWHM} \simeq 1.4$ and large distances $|x| \gtrsim 20$ where the autocorrelation reaches unity. This dependency

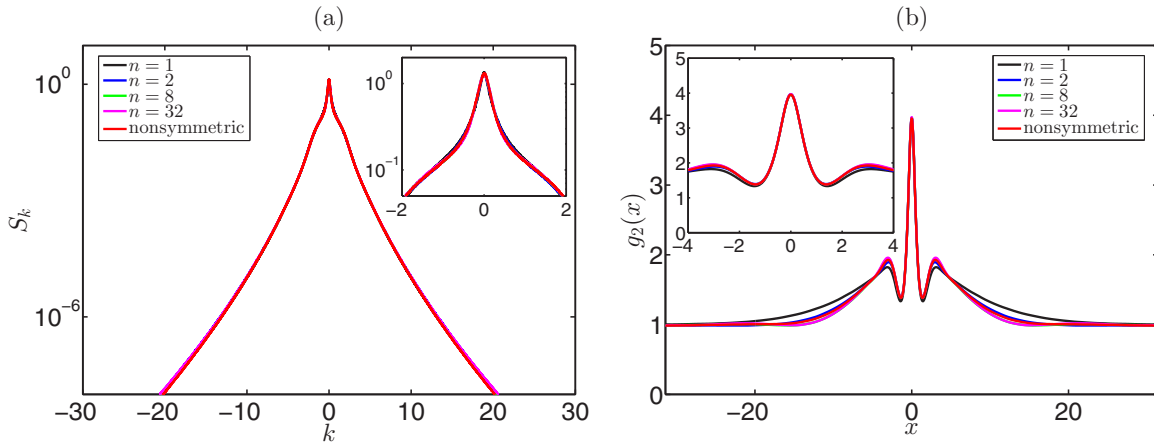


FIG. 11. Ensemble- and time-averaged statistical functions in the beginning of the QSS for four super-Gaussian initial spectra with the exponents $n = 1, 2, 8, 32$ and one nonsymmetric initial spectrum: (a) the wave-action spectrum S_k and (b) the autocorrelation of intensity $g_2(x)$. The initial nonlinearity strength is $\alpha_0 = 64$ for the four super-Gaussian spectra and $\alpha_0 \approx 65.2$ for the nonsymmetric spectrum. The insets show the same functions as in the main figures with smaller scales.

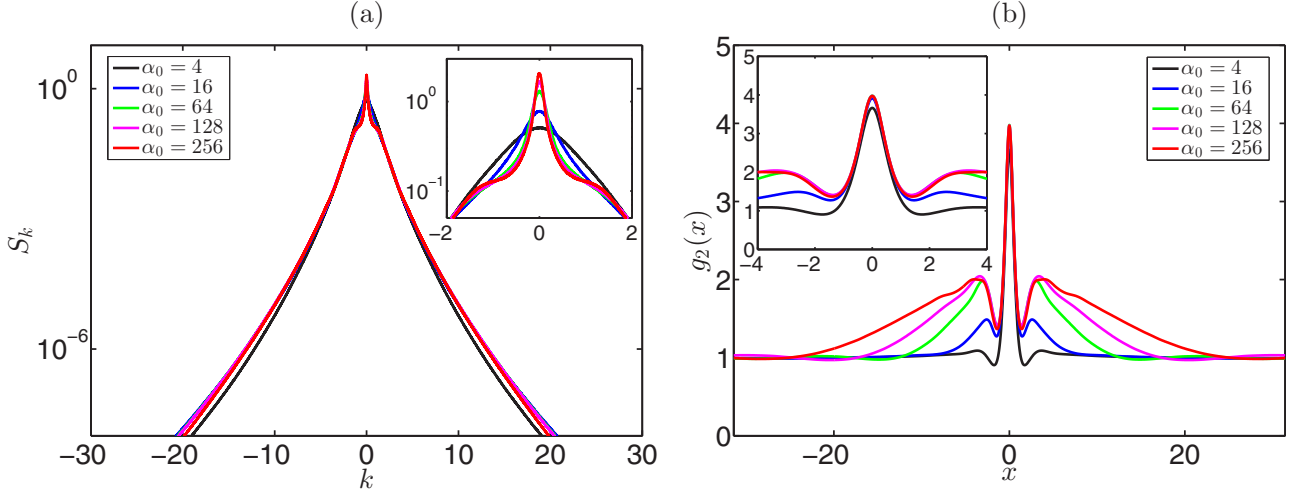


FIG. 12. Ensemble- and time-averaged statistical functions in the beginning of the QSS for different initial nonlinearity levels $\alpha_0 = 4, 16, 64, 128,$ and 256 : (a) the wave-action spectrum S_k and (b) the autocorrelation of intensity $g_2(x)$. The initial spectrum is super-Gaussian with the exponent $n = 32$. The insets show the same functions as in the main figures with smaller scales.

means that the integrable system “feels” the shape of the initial spectrum even when it is very narrow.

The dependency of statistical functions on the level of initial nonlinearity (i.e., spectral width) is more pronounced. In particular, the wave-action spectrum changes with α_0 most noticeably at small wave numbers $|k| \lesssim 1$, Fig. 12(a), where the spectrum forms a triangular that sharpens with increasing α_0 . For sufficiently large α_0 , the spectrum at these wave numbers resembles the asymptotic spectrum of the noise-induced MI [25]. Note that the spectra for the smallest values of initial nonlinearity $\alpha_0 = 4$ and 16 presented in Fig. 12(a) are very similar to the spectrum obtained in Ref. [33] for the pure PCW and the largest correlation length $L_c = 1.8$ studied in that paper.

The autocorrelation of intensity $g_2(x)$ keeps its universal bell-shaped profile at small distances $|x| \lesssim 1.4$, while changing significantly with α_0 at intermediate distances where it approaches to unity [Fig. 12(b)]. The distance where the autocorrelation practically reaches unity increases with α_0 roughly as $|x| \propto \sqrt{\alpha_0}$, as can be seen in the figure [compare $g_2(x)$ for $\alpha_0 = 4, 16, 64,$ and 256]. Note that for $\alpha_0 = 4$ the maximum of the autocorrelation function is slightly smaller than 4, which reflects the smaller value of the fourth-order moment κ_4 in the QSS for this experiment; see Figs. 3(b) and 5.

APPENDIX D: TIME AND ENSEMBLE AVERAGING VERSUS ENSEMBLE AVERAGING

In this Appendix, we compare time and ensemble averaging in the beginning of the QSS versus ensemble averaging only for four statistical functions: the moments, the PDF of intensity, the wave-action spectrum, and the autocorrelation of intensity. As one can see in Fig. 13, the statistical functions with and without time averaging differ only marginally. The two significant distinctions consist in (i) slightly elevated values of the higher order moments at $t = 20$ compared to $t = 40$ and time-averaged moments [see the inset in Fig. 13(a)] and

(ii) the higher accuracy in measurement of the PDF when the time-averaging is applied [see Fig. 13(b)] that highlights the main advantage of this technique. Hence, we conclude that in the QSS the considered statistical functions change with time very slowly, and the averaging within relatively short time intervals can be used to improve accuracy of our results.

APPENDIX E: EFFECTS OF AN ADDITIONAL WIDE-SPECTRUM NOISE

In the main part of the paper, we have examined integrable turbulence developing from PCW of narrowband spectrum. However, real physical systems have noise that may change the spectral “portrait” of initial conditions and affect our results. In this Appendix, we demonstrate two numerical experiments with inclusion of additional wide-spectrum noise of small and moderate levels and discuss effects on the statistical results.

The initial conditions for both experiments represent a sum of two PCW,

$$\psi_0(x) = \frac{\psi^{(1)}(x) + \chi \psi^{(2)}(x)}{\sqrt{1 + \chi^2}}, \quad (\text{E1})$$

where $\psi^{(1,2)}$ are determined from Eqs. (18) and (19); the average intensity of these PCW is unity, $\langle |\psi^{(1,2)}|^2 \rangle = 1$. In Eq. (E1), $\psi^{(1)}$ is the (original) narrowband PCW with super-Gaussian spectrum with the exponent $n = 32$ and nonlinearity strength $\alpha_0 = 64$, and $\psi^{(2)}$ is a wide-spectrum wave modeling noise, while the parameter χ sets the average noise amplitude in the x space.

For the first experiment with small noise level, we use noise amplitude $\chi = 10^{-3}$ and super-Gaussian spectrum for $\psi^{(2)}$ with the exponent $n = 32$ and spectral width $\theta = 4$; see Eqs. (18) and (19). For the second experiment, we set these parameters at $\chi = 10^{-1}$, $n = 32$ and $\theta = 8$. The left inset in Fig. 14(c) illustrates the initial wave-action spectrum S_k at $t = 0$ for these two additional experiments with green and red lines, in comparison with the original experiment without

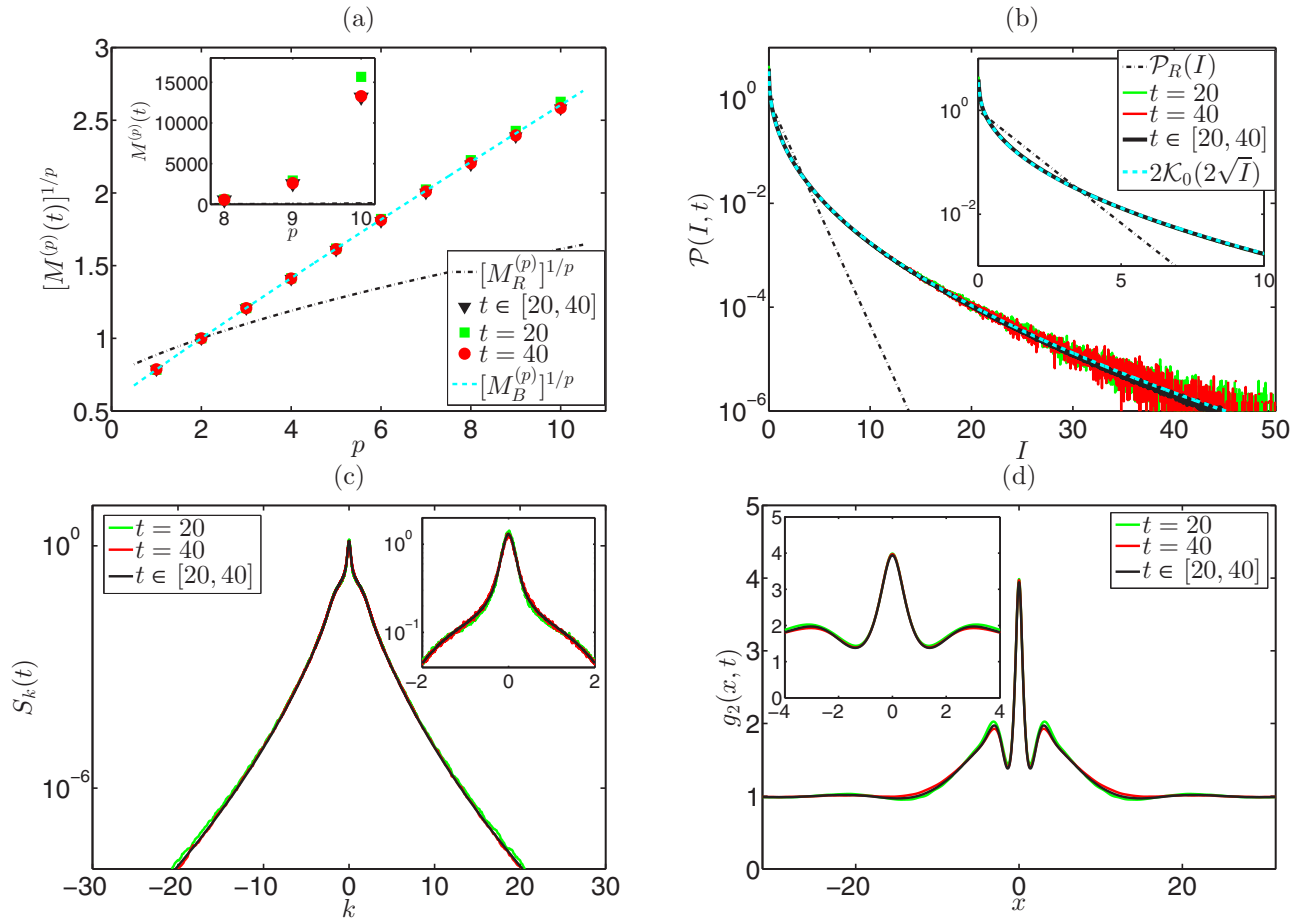


FIG. 13. Time- and ensemble averaging vs ensemble averaging for four statistical functions: (a) the moments $[M^{(p)}]^{1/p}$, (b) the PDF of relative wave intensity $\mathcal{P}(I)$, (c) the wave-action spectrum S_k , and (d) the autocorrelation of intensity $g_2(x)$. Time- and ensemble-averaged functions with time averaging in the interval $t \in [20, 40]$ are shown with black, while ensemble-averaged functions at times $t = 20$ and $t = 40$ are shown with green and red, respectively. The initial spectrum is super-Gaussian with the exponent $n = 32$ and nonlinearity strength $\alpha_0 = 64$. In panels (b) and (a), the black dash-dotted lines indicate the exponential PDF (2) and the corresponding moments (17), while the cyan dashed lines indicate the Bessel PDF (24) and the corresponding moments (25). The inset in panel (a) shows the higher order moments $M^{(p)}$ (without the $1/p$ power), while the insets in panels (b)–(d) show the same functions as in the main figures with smaller scales.

noise (black line). As in the case of the original experiment, all statistical characteristics discussed below are averaged over the ensemble of 1000 random realizations of initial conditions and those statistical functions that relate to the QSS, additionally over time interval $t \in [20, 40]$ accommodated in the beginning of the QSS.

As shown in Fig. 14, results for the first experiment with small additional noise practically coincide with those for the original experiment without noise. The largest distinctions that we observe are very small deviations of the PDF at large intensities, together with by less than 10% smaller value of the tenth-order moment $M^{(10)}$; see the inset in Fig. 14(b). As we have mentioned earlier, differences of the same order appear when we repeat an experiment using another 1000 random realizations of the initial data. For this reason, we think that the observed discrepancies come mainly from finiteness and randomness of the ensemble of initial conditions and disregard them.

Stronger effects are observed for the second experiment with moderate noise level. In this case, the difference is seen already for the transient regime, in which the fourth-order

moment starts to increase noticeably earlier and reaches smaller maximum value at slightly different time compared to the original experiment without noise [Fig. 14(a)]. In the QSS, the fourth-order moment and the potential energy reach the same values, $\kappa_4 \approx 4$ and $\langle H_{nl} \rangle \approx -2$, as without noise; however, the kinetic energy becomes larger, $\langle H_I \rangle \approx 1.2$ versus $\langle H_I \rangle \approx 1$ without noise. The moments practically coincide with those for the experiment without noise [Fig. 14(b)]; the measured value for the tenth-order moment $M^{(10)}$ turns out to be about 10% smaller than without noise.

Note that in the presence of noise, the initial kinetic energy $\langle H_I \rangle|_{t=0} \approx 0.2$ is also larger than that without noise, $\langle H_I \rangle|_{t=0} \approx 0$, by approximately the same value as in the QSS. The corresponding contribution to the initial kinetic energy comes from wave numbers $|k| \simeq 8$, where noise has intensity in the k space $|\psi_k^{(2)}|^2/\Delta k \approx 6.5 \times 10^{-4}$; see the left inset in Fig. 14(c). Calculating the integral sum for the kinetic energy in the k space in Eq. (9), one can easily get the difference of $\simeq 0.2$ originating from this effect.

The wave-action spectrum in the beginning of the QSS is affected by noise very slightly at small wave numbers $|k| \lesssim 1$

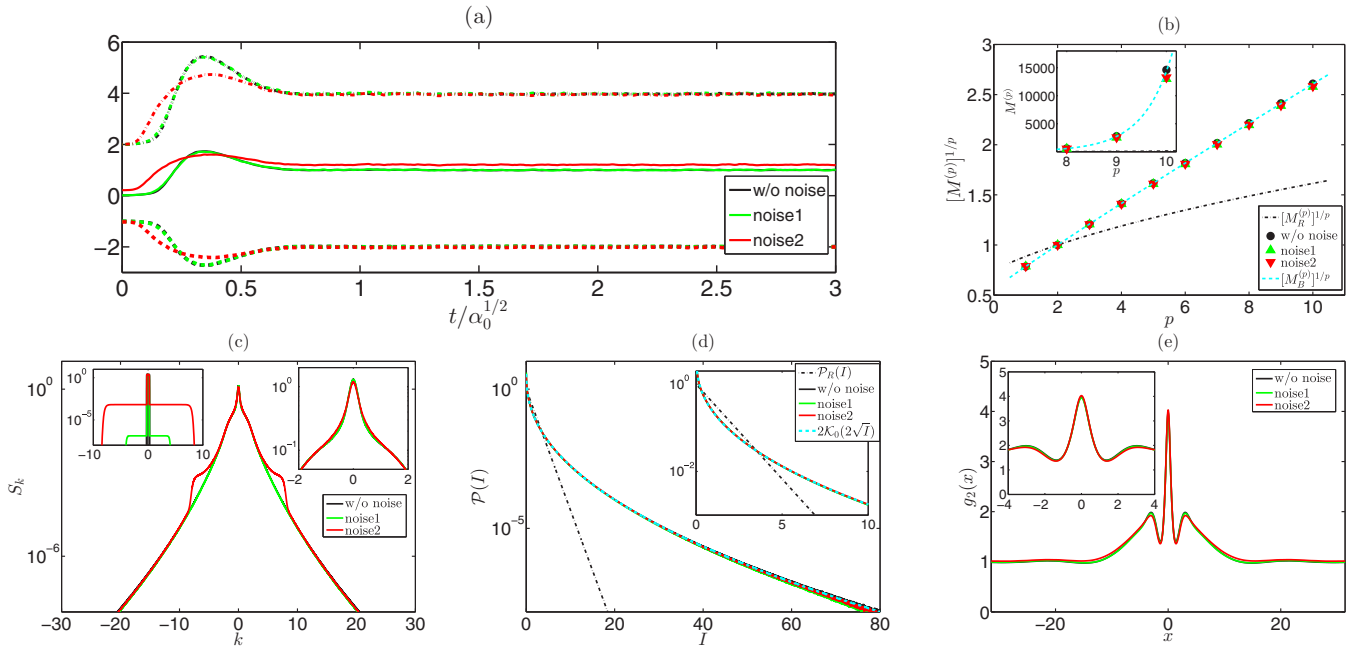


FIG. 14. Influence of an additional wide-spectrum noise on the statistics. The black lines indicate the original experiment with super-Gaussian initial spectrum with the exponent $n = 32$ and nonlinearity strength $\alpha_0 = 64$, the green lines indicate the experiment with additional small noise (E1) with amplitude $\chi = 10^{-3}$ and super-Gaussian spectrum with $n = 32$ and $\theta = 4$, and the red lines indicate the one with moderate noise $\chi = 10^{-1}$, $n = 32$, and $\theta = 8$. (a) Evolution of the ensemble-averaged kinetic energy $\langle H_I \rangle$ (thin solid lines), potential energy $\langle H_{nl} \rangle$ (thick dashed lines), and the fourth-order moment κ_4 (thick dash-dotted lines). [(b)–(e)] Ensemble- and time-averaged statistical characteristics in the beginning of the QSS: (b) the moments $[M^{(p)}]^{1/p}$, (c) the wave-action spectrum S_k , (d) the PDF $\mathcal{P}(I)$, and (e) the autocorrelation of intensity $g_2(x)$. The inset in panel (b) shows the higher order moments $M^{(p)}$ (without the $1/p$ power), the left inset in panel (c) shows the initial wave-action spectrum at $t = 0$, and the right inset in the same panel together with the insets in panels (d) and (e) show the same functions as in the main figures with smaller scales. In panels (d) and (b), the black dash-dotted lines indicate the exponential PDF (2) and the corresponding moments (17), while the cyan dashed lines indicate the Bessel PDF (24) and the corresponding moments (25).

and significantly at wave numbers $|k| \simeq 8$ where the spectrum acquires “wings” approximately at the level $S_k \simeq 6 \times 10^{-4}$ of the initial noise; see Fig. 14(c). These “wings” are the source for larger value of the kinetic energy $\langle H_I \rangle$ in the QSS, compared to the experiment without noise. The PDF and the autocorrelation of intensity turn out to be practically unaffected by noise in the second experiment [Figs. 14(d) and 14(e)].

We conclude that a significant additional noise may noticeably change the transient regime, modify the wave-action spectrum with “wings” appearing at the noise level, and increase the kinetic energy. However, even with notable noise levels, it leaves the potential energy, the moments, the PDF and the autocorrelation of intensity practically unaffected in the QSS. In our opinion, this opens possibilities for experimental observation of the latter statistical functions.

[1] C. Kharif and E. Pelinovsky, *Eur. J. Mech. B* **22**, 603 (2003).
 [2] K. Dysthe, H. E. Krogstad, and P. Muller, *Annu. Rev. Fluid Mech.* **40**, 287 (2008).
 [3] M. Onorato, S. Residori, U. Bortolozzo, A. Montina, and F. T. Arecchi, *Phys. Rep.* **528**, 47 (2013).
 [4] J. M. Dudley, G. Genty, A. Mussot, A. Chabchoub, and F. Dias, *Nat. Rev. Phys.* **1**, 675 (2019).
 [5] D. H. Peregrine, *J. Aust. Math. Soc. Series B* **25**, 16 (1983).
 [6] N. N. Akhmediev, V. M. Eleonskii, and N. E. Kulagin, *Teoret. Mat. Fiz.* **72**, 183 (1987).
 [7] N. Akhmediev, A. Ankiewicz, and J. M. Soto-Crespo, *Phys. Rev. E* **80**, 026601 (2009).
 [8] E. A. Kuznetsov, *DoSSR* **236**, 575 (1977).
 [9] Y.-C. Ma, *Stud. Appl. Math.* **60**, 43 (1979).
 [10] A. A. Gelash and V. E. Zakharov, *Nonlinearity* **27**, R1 (2014).
 [11] B. Kibler, J. Fatome, C. Finot, G. Millot, F. Dias, G. Genty, N. Akhmediev, and J. M. Dudley, *Nat. Phys.* **6**, 790 (2010).
 [12] A. Chabchoub, N. P. Hoffmann, and N. Akhmediev, *Phys. Rev. Lett.* **106**, 204502 (2011).
 [13] H. Bailung, S. K. Sharma, and Y. Nakamura, *Phys. Rev. Lett.* **107**, 255005 (2011).
 [14] A. Chabchoub, N. Hoffmann, M. Onorato, and N. Akhmediev, *Phys. Rev. X* **2**, 011015 (2012).
 [15] A. Chabchoub, N. Hoffmann, M. Onorato, A. Slunyaev, A. Sergeeva, E. Pelinovsky, and N. Akhmediev, *Phys. Rev. E* **86**, 056601 (2012).
 [16] B. Kibler, J. Fatome, C. Finot, G. Millot, G. Genty, B. Wetzler, N. Akhmediev, F. Dias, and J. M. Dudley, *Sci. Rep.* **2**, 463 (2012).

- [17] B. Kibler, A. Chabchoub, A. Gelash, N. Akhmediev, and V. E. Zakharov, *Phys. Rev. X* **5**, 041026 (2015).
- [18] M. Onorato, A. R. Osborne, M. Serio, and S. Bertone, *Phys. Rev. Lett.* **86**, 5831 (2001).
- [19] S. Nazarenko, *Wave Turbulence*, Lecture Notes in Physics, Vol. 825 (Springer, Berlin, 2011).
- [20] L. Mandel and E. Wolf, *Optical Coherence and Quantum Optics* (Cambridge University Press, Cambridge, UK, 1995).
- [21] R. El Koussaifi, A. Tikan, A. Toffoli, S. Randoux, P. Suret, and M. Onorato, *Phys. Rev. E* **97**, 012208 (2018).
- [22] V. E. Zakharov and A. B. Shabat, *Sov. Phys. JETP* **34**, 62 (1972).
- [23] S. Novikov, S. V. Manakov, L. P. Pitaevskii, and V. E. Zakharov, *Theory of Solitons: The Inverse Scattering Method* (Springer Science & Business Media, New York, 1984).
- [24] V. E. Zakharov, *Stud. Appl. Math.* **122**, 219 (2009).
- [25] D. S. Agafontsev and V. E. Zakharov, *Nonlinearity* **28**, 2791 (2015).
- [26] A. E. Kraych, D. Agafontsev, S. Randoux, and P. Suret, *Phys. Rev. Lett.* **123**, 093902 (2019).
- [27] D. S. Agafontsev and V. E. Zakharov, *Nonlinearity* **29**, 3551 (2016).
- [28] P. Walczak, S. Randoux, and P. Suret, *Phys. Rev. Lett.* **114**, 143903 (2015).
- [29] M. Onorato, A. R. Osborne, M. Serio, and T. Damiani, *Rogue Wave 2000*, 181 (2000).
- [30] M. Onorato, A. R. Osborne, M. Serio, L. Cavaleri, C. Brandini, and C. T. Stansberg, *Phys. Rev. E* **70**, 067302 (2004).
- [31] M. Onorato, A. R. Osborne, M. Serio, L. Cavaleri, C. Brandini, and C. T. Stansberg, *Eur. J. Mech. B* **25**, 586 (2006).
- [32] J. M. Soto-Crespo, N. Devine, and N. Akhmediev, *Phys. Rev. Lett.* **116**, 103901 (2016).
- [33] N. Akhmediev, J. M. Soto-Crespo, and N. Devine, *Phys. Rev. E* **94**, 022212 (2016).
- [34] P. Suret, R. El Koussaifi, A. Tikan, C. Evain, S. Randoux, C. Szwaj, and S. Bielawski, *Nat. Commun.* **7**, 13136 (2016).
- [35] A. Tikan, S. Bielawski, C. Szwaj, S. Randoux, and P. Suret, *Nat. Photon.* **12**, 228 (2018).
- [36] F. Copie, S. Randoux, and P. Suret, *Rev. Phys.* **5**, 100037 (2020).
- [37] G. P. Agrawal, *Nonlinear Fiber Optics* (Academic Press, San Diego, 2001).
- [38] M. Onorato, D. Proment, G. El, S. Randoux, and P. Suret, *Phys. Lett. A* **380**, 3173 (2016).
- [39] S. Randoux, F. Gustave, P. Suret, and G. El, *Phys. Rev. Lett.* **118**, 233901 (2017).
- [40] M. Bertola and A. Tovbis, *Commun. Pure Appl. Math.* **66**, 678 (2013).
- [41] A. Tikan, C. Billet, G. El, A. Tovbis, M. Bertola, T. Sylvestre, F. Gustave, S. Randoux, G. Genty, P. Suret, and J. M. Dudley, *Phys. Rev. Lett.* **119**, 033901 (2017).
- [42] A. Tikan, *Phys. Rev. E* **101**, 012209 (2020).
- [43] G. Roberti, G. El, S. Randoux, and P. Suret, *Phys. Rev. E* **100**, 032212 (2019).
- [44] A. Tikan, S. Randoux, G. El, A. Tovbis, F. Copie, and P. Suret, *Front. Phys.* **8**, 599435 (2021).
- [45] T. Kokina and F. Dias, *J. Mar. Sci. Eng.* **8**, 1023 (2020).
- [46] E. M. Bitner-Gregersen, O. Gramstad, A. K. Magnusson, and M. P. Malila, *Ocean Dyn.* **71**, 81 (2021).
- [47] W. S. Cleveland, S. J. Devlin, and E. Grosse, *J. Econom.* **37**, 87 (1988).
- [48] A. Mathis, L. Froehly, S. Toenger, F. Dias, G. Genty, and J. M. Dudley, *Sci. Rep.* **5**, 1 (2015).
- [49] A. Safari, R. Fickler, M. J. Padgett, and R. W. Boyd, *Phys. Rev. Lett.* **119**, 203901 (2017).